

# Sensorless Control of Induction Motor Drives

JOACHIM HOLTZ, FELLOW, IEEE

## Invited Paper

Controlled induction motor drives without mechanical speed sensors at the motor shaft have the attractions of low cost and high reliability. To replace the sensor, the information on the rotor speed is extracted from measured stator voltages and currents at the motor terminals. Vector-controlled drives require estimating the magnitude and spatial orientation of the fundamental magnetic flux waves in the stator or in the rotor. Open-loop estimators or closed-loop observers are used for this purpose. They differ with respect to accuracy, robustness, and sensitivity against model parameter variations. Dynamic performance and steady-state speed accuracy in the low-speed range can be achieved by exploiting parasitic effects of the machine. The overview in this paper uses signal flow graphs of complex space vector quantities to provide an insightful description of the systems used in sensorless control of induction motors.

**Keywords**—Adaptive tuning, complex state variables, identification, induction motor, modeling, observers, sensorless control, vector control.

## NOMENCLATURE

All variables are normalized unless stated otherwise.

$\underline{1}, a, a^2$	Unity vector rotators.
$a, b, c$	Stator phase axes.
$A$	Current density, MMF.
$D$	Denominator.
$f$	Function of complex space harmonics.
$\underline{f}$	Field position vector.
$f$	Frequency.
$G$	Observer tensor.
$i_d$	Direct axis current signal.
$i_q$	Quadrature axis current signal.
$I_{ph}$	Nonnormalized rms phase current.
$\underline{i}_s$	Stator current vector.
$\underline{i}_u$	Unbalance current vector.
$\underline{i}_z$	Disturbance current vector.
$\underline{i}_2$	Saturation current vector.
$k_s$	Coupling factor of the stator winding.
$k_r$	Coupling factor of the rotor winding.
$l_m$	Mutual inductance.
$m_{s1}$	Mutual inductance.

$l_r$	Rotor inductance.
$l_s$	Stator inductance.
$N$	Number of rotor bars.
$N$	Numerator.
$p$	Number of pole pairs.
$q$	Instantaneous reactive power.
$r_s$	Stator resistance.
$r_r$	Rotor resistance.
$r'_\sigma$	Effective transient resistance.
$s$	Laplace variable.
$\text{sec}(\underline{i}_s)$	Sector indicator vector.
$T_e$	Electromagnetic torque.
$T_L$	Load torque.
$u_d$	DC link voltage.
$u_i$	Rotor-induced voltage.
$u_{sl}$	Rotor slot harmonics voltage.
$u_{ss}$	Zero sequence voltage.
$u_\sigma$	Leakage-dependent zero sequence voltage.
$U_{ph}$	Nonnormalized rms phase voltage.
$\underline{u}_{ir}$	Vector of the rotor induced voltage.
$\underline{u}_s$	Stator voltage vector.
$u_\sigma$	Zero sequence voltage.
$\underline{u}_z$	Disturbance voltage vector.
$\underline{u}_1 \cdots \underline{u}_6$	Switching state vectors.
$Z$	High-frequency impedance.
1, 2	Sequence in a vector product.

## Greek Symbols

$\alpha$	Circumferential position angle.
$\delta$	Field angle.
$\varepsilon$	Error angle.
$\gamma$	Stator current angle.
$\gamma$	Field alignment error.
$\gamma_u$	Error angle of carrier voltage.
$\gamma_i$	Error angle of carrier current.
$\vartheta$	Rotor position angle.
$\varphi$	Phase displacement angle.
$\sigma$	Total leakage factor.
$\sigma l_s$	Total leakage inductance.
$\tau$	Normalized time.
$\tau_m$	Mechanical time constant.
$\tau_r$	Rotor time constant.

Manuscript received September 3, 2001; revised March 11, 2002.

The author is with the Electrical Machines and Drives Group, Wuppertal University, 42119 Wuppertal, Germany (j.holtz@ieee.org).

Publisher Item Identifier 10.1109/JPROC.2002.800726.

$\tau_s$	Stator time constant.
$\omega_r$	Rotor slip frequency.
$\omega_s$	Stator fundamental excitation frequency.
$\omega_k$	Frequency of $k$ -coordinates.
$\omega$	Angular mechanical velocity of the equivalent two-pole machine.
$\psi_r$	Rotor flux linkage vector.
$\psi_s$	Stator flux linkage vector.
$\psi_\sigma$	Leakage flux linkage vector.

#### Subscripts

$\alpha, \beta$	Components in stator coordinates.
$a, b, c$	Phases, winding axes.
$av$	Average value.
$c$	Carrier.
$d, q$	Synchronous coordinates.
$k$	$k$ -coordinates.
max	Maximum value.
min	Minimum value.
$n$	Negative sequence.
$p$	Positive sequence.
$ph$	Per phase value.
$r$	Rotor.
$R$	Rated value.
$s$	Stator.
$sat$	Saturation.
$sl, slot$	Slotting effect.
$z$	$z$ component of a vector product.
$x, y$	$xy$ -coordinates.
$\sigma$	Leakage fluxes.
1	Fundamental quantity.

#### Superscripts

$(S)$	In stator coordinates.
$(F)$	In field coordinates.
$(C)$	In current coordinates.
$(X)$	In $xy$ -coordinates.
$S, R$	Originates from stator (rotor) model.
*	Reference value.
$\bar{\phantom{x}}$	Average value.
$\hat{\phantom{x}}$	Estimated value.
$\wedge$	Peak amplitude.
$\sim$	Laplace transform.
$'$	Marks transient time constants.
$\prime$	Precedes a nonnormalized variable.

## I. INTRODUCTION

AC drives based on full digital control have reached the status of a mature technology. The world market volume is about 12 000 million US\$ with an annual growth rate of 15%.

Ongoing research has concentrated on the elimination of the speed sensor at the machine shaft without deteriorating the dynamic performance of the drive control system [1]. Speed estimation is an issue of particular interest with induction motor drives where the mechanical speed of the rotor is generally different from the speed of the revolving

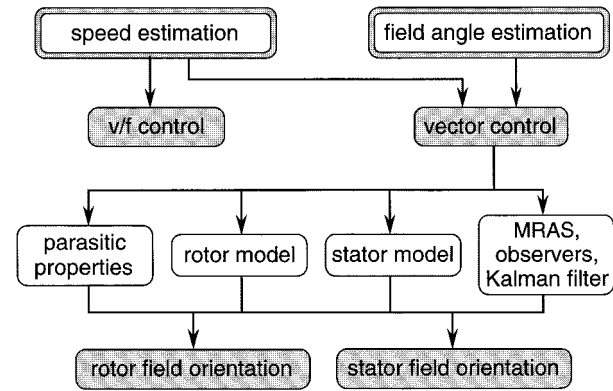


Fig. 1. Methods of sensorless speed control.

magnetic field. The advantages of speed-sensorless induction motor drives are reduced hardware complexity and lower cost, reduced size of the drive machine, elimination of the sensor cable, better noise immunity, increased reliability, and less maintenance requirements. Operation in hostile environments mostly requires a motor without speed sensor.

A variety of different solutions for sensorless ac drives have been proposed in the past few years. Their merits and limits are reviewed based on a survey of the available literature.

Fig. 1 gives a schematic overview of the methodologies applied to speed-sensorless control. A basic approach requires only a speed estimation algorithm to make a rotational speed sensor obsolete. The  $v/f$  control principle adjusts a constant V/Hz ratio of the stator voltage by feedforward control. It serves to maintain the magnetic flux in the machine at a desired level. Its simplicity satisfies only moderate dynamic requirements. High dynamic performance is achieved by field orientation, also called vector control. The stator currents are injected at a well-defined phase angle with respect to the spatial orientation of the rotating magnetic field, thus overcoming the complex dynamic properties of the induction motor. The spatial location of the magnetic field, the field angle, is difficult to measure. There are various types of models and algorithms used for its estimation, as shown in the lower portion of Fig. 1. Control with field orientation may either refer to the rotor field or to the stator field, where each method has its own merits.

Discussing the variety of different methods for sensorless control requires an understanding of the dynamic properties of the induction motor which is treated in a first introductory section.

## II. INDUCTION MACHINE DYNAMICS

### A. An Introduction to Space Vectors

The use of space vectors as complex state variables is an efficient method for ac machine modeling [2], [37]. The space vector approach represents the induction motor as a dynamic system of only third order and permits an insightful visualization of the machine and the superimposed control structures by complex signal flow graphs [3]. Such signal flow graphs will be used throughout this paper. The approach implies that the spatial distributions along the airgap of the

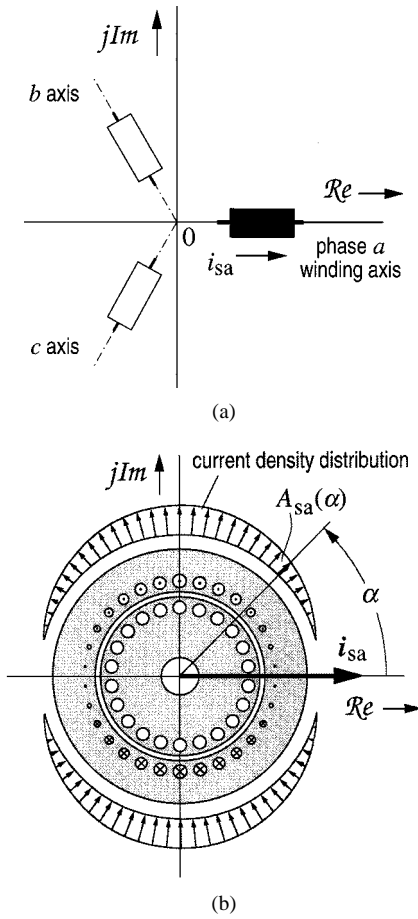


**Fig. 2.** Stator winding with only phase *a* energized. (a) Symbolic representation. (b) Generated current density distribution.

magnetic flux density, the flux linkages, and the current densities (magnetomotive force, MMF) are sinusoidal. Linear magnetics are assumed while iron losses, slotting effects, and deep bar and end effects are neglected.

To describe the space vector concept, a three-phase stator winding is considered, as shown in Fig. 2(a) in a symbolic representation. The winding axis of phase *a* is aligned with the real axis of the complex plane. To create a sinusoidal flux density distribution, the stator MMF must be a sinusoidal function of the circumferential coordinate. The distributed phase windings of the machine model are therefore assumed to have sinusoidal winding densities. Each phase current then creates a specific sinusoidal MMF distribution, the amplitude of which is proportional to the respective current magnitude, while its spatial orientation is determined by the direction of the respective phase axis and the current polarity. For example, a positive current  $i_{sa}$  in stator phase *a* creates a sinusoidal current density distribution that leads the windings axis *a* by 90°, therefore having its maximum in the direction of the imaginary axis, as shown in Fig. 2(b).

The total MMF in the stator is obtained as the superposition of the current density distributions of all three phases. It is again a sinusoidal distribution, which is indicated in Fig. 3 by the varying diameter of the conductor cross sections or, in an equivalent representation, by two half-moon-shaped segments. Amplitude and spatial orientation of the total MMF depend on the respective magnitudes of the phase

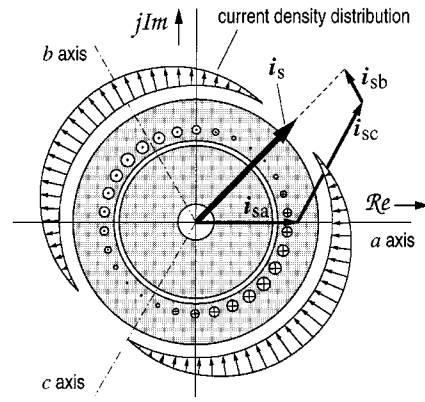


**Fig. 3.** Current density distribution resulting from the phase currents  $i_{sa}$ ,  $i_{sb}$ , and  $i_{sc}$ .

currents  $i_{sa}$ ,  $i_{sb}$ , and  $i_{sc}$ . As the phase currents vary with time, the generated current density profile displaces in proportion, forming a rotating current density wave.

The **superposition** of the current density profiles of the individual phases can be represented by the spatial addition of the contributing phase currents. For this purpose, the phase currents need to be transformed into space vectors by imparting them the spatial orientation of the pertaining phase axes. The resulting equation

$$\mathbf{i}_s = \frac{2}{3} (\mathbf{1}i_{sa} + a i_{sb} + a^2 i_{sc}) \quad (1)$$

defines the complex stator current space vector  $\mathbf{i}_s$ . Note that the three terms on the right-hand side of (1) are also complex space vectors. Their magnitudes are determined by the instantaneous value of the respective phase current, their spatial orientations by the direction of the respective winding axis. The first term in (1), though complex, is real-valued since the winding axis of phase *a* is the real axis of the reference frame. It is normally omitted in the notation of (1) to characterize the real axis by the unity vector  $\mathbf{1} = e^{j0}$ . As a complex quantity, the space vector  $\mathbf{1} \cdot i_{sa}$  represents the sinusoidal current density distribution generated by the phase current  $i_{sa}$ . Such distribution is represented in Fig. 2(b). In the second term of (1),  $a = \exp(j2\pi/3)$  is a unity vector that indicates the direction of the winding axis of phase *b*, and hence  $a i_{sb}$  is the space vector that represents the sinusoidal current density distribution generated by the phase current  $i_{sb}$ . Likewise does  $a^2 i_{sc}$  represent the current density distribution generated by  $i_{sc}$ , with  $a^2 = \exp(j4\pi/3)$  indicating the direction of the winding axis of phase *c*.

Being a complex quantity, the stator current space vector  $\mathbf{i}_s$  in (1) represents the sinusoidal spatial distribution of the total MMF wave created *inside* the machine by the three phase currents that flow *outside* the machine. The MMF wave has its maximum at an angular position that leads the current space vector  $\mathbf{i}_s$  by 90°, as illustrated in Fig. 3. Its amplitude is proportional to  $i_s = |\mathbf{i}_s|$ .

The scaling factor 2/3 in (1) reflects the fact that the total current density distribution is obtained as the superposition of the current density distributions of three phase windings while the contribution of only two phase windings, spaced 90° apart, would have the same spatial effect with the phase current properly adjusted. The factor 2/3 also ensures that the

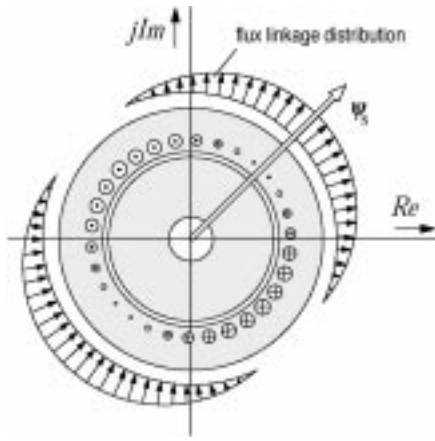


**Fig. 4.** Flux density distribution resulting from the stator currents in Fig. 3.

contributing phase currents  $i_{sa}$ ,  $i_{sb}$ , and  $i_{sc}$  can be readily reconstructed as the projections of  $\mathbf{i}_s$  on the respective phase axes, hence

$$\begin{aligned} i_{sa} &= \text{Re}\{\mathbf{i}_s\} \\ i_{sb} &= \text{Re}\{a^2 \cdot \mathbf{i}_s\} \\ i_{sc} &= \text{Re}\{a \cdot \mathbf{i}_s\}. \end{aligned} \quad (2)$$

Equation (2) holds on the condition that zero sequence currents do not exist. This is always true since the winding star point of an inverter-fed induction motor is never connected [4].

In steady-state operation, the stator phase currents form a balanced, sinusoidal three-phase system which cause the stator MMF wave to rotate at a constant amplitude in synchronism with the angular frequency  $\omega_s$  of the stator currents.

The flux density distribution in the airgap is obtained by spatial integration of the current density wave. It is therefore also a sinusoidal wave, and it lags the current density wave by  $90^\circ$ , as illustrated in Fig. 4. It is convenient to choose the flux *linkage* wave as a system variable instead of the flux *density* wave as the former contains added information on the winding geometry and the number of turns. By definition, a flux linkage distribution has the same spatial orientation as the pertaining flux density distribution. The stator flux linkage distribution in Fig. 4 is therefore represented by the space vector  $\psi_s$ .

A rotating flux density wave induces voltages in the individual stator windings. Since the winding densities are sinusoidal spatial functions, the induced voltages are also sinusoidally distributed in space. The same is true for the resistive voltage drop in the windings. The total of both distributed voltages in all phase windings is represented by the stator voltage space vector  $\mathbf{u}_s$ , which is a complex variable. Against this, the phase voltages at the machine terminals are discrete, scalar quantities. They define the stator voltage space vector

$$\mathbf{u}_s = \frac{2}{3} (u_{sa} + a u_{sb} + a^2 u_{sc}) \quad (3)$$

in the same way as the phase currents define the stator current space vector in (1).

Note that current space vectors are defined in a different way than flux linkage vectors: they are always  $-90^\circ$  out of phase with respect to the maximum of the current density distribution they represent (see Fig. 3). Against this, flux linkage vectors are always aligned with the maximum of the respective flux linkage distribution (see Fig. 4). This is a convenient definition, permitting to establish a simple relationship between both vectors, for instance,  $\psi_s = l_s \mathbf{i}_s$ , where  $l_s$  is the three-phase inductance of the stator winding. The three-phase inductance of a distributed winding is 1.5 times the per phase inductance of that very winding [2], [36].

## B. Machine Equations

To establish the machine equations, all physical quantities are considered normalized, and rotor quantities are referred to the stator, i.e., scaled in magnitude by the stator to rotor winding ratio. A table of the base quantities used for normalization is given in the Appendix. The normalization includes the conversion of machines of arbitrary number  $p$  of pole pairs to the two-pole equivalent machine that is shown in the illustrations. It has been found convenient to normalize time as  $\tau = \omega_{sR} t$ , where  $\omega_{sR}$  is the rated stator frequency of the machine.

A rotating coordinate system is chosen to establish the voltage equations of the induction motor. This coordinate system rotates at an angular stator velocity  $\omega_k$ , where the value of  $\omega_k$  is left unspecified to be as general as possible. Of course, when a specific solution of the system equations is sought, the coordinate system must be defined first.

The stator voltage equation in the general  $k$ -coordinate system is

$$\mathbf{u}_s = r_s \mathbf{i}_s + \frac{d\psi_s}{d\tau} + j\omega_k \psi_s \quad (4)$$

where  $r_s \mathbf{i}_s$  is the resistive voltage drop and  $r_s$  is the stator resistance. The sum of the last two terms in (4) represents the induced voltage, or back electromagnetic force (EMF), of which  $d\psi_s/d\tau$  is the stationary term that accounts for the variations in time of the stator flux linkage, as seen from the moving reference frame. The second term  $j\omega_k \psi_s$  is the motion-induced voltage that results from the varying displacement of the winding conductors with respect to the reference frame.

In the rotor, this displacement is  $\omega_k - \omega$ , where  $\omega$  is the angular mechanical velocity of the rotor, and hence the rotor voltage equation is

$$0 = r_r \mathbf{i}_r + \frac{d\psi_r}{d\tau} + j(\omega_k - \omega) \psi_r. \quad (5)$$

The left-hand side shows that the rotor voltage sums up to zero in a squirrel cage induction motor.

Equations (4) and (5) represent the electromagnetic subsystem of the machine as a second-order dynamic system by two state equations, however, in terms of four state variables:  $\mathbf{i}_s$ ,  $\psi_s$ ,  $\mathbf{i}_r$ ,  $\psi_r$ . Therefore, two flux linkage equations

$$\psi_s = l_s \mathbf{i}_s + l_m \mathbf{i}_r \quad (6)$$

$$\psi_r = l_m \mathbf{i}_s + l_r \mathbf{i}_r \quad (7)$$



are needed to establish completeness. In (6) and (7),  $l_s$  is the stator inductance,  $l_r$  is the rotor inductance, and  $l_m$  is the mutual inductance between the stator and the rotor winding; all inductances are three-phase inductances having 1.5 times the value of the respective phase inductances.

Equations (4) and (5) are easily transformed to a different reference frame by just substituting  $\omega_k$  with the angular velocity of the respective frame. To transform the equations to the stationary reference frame, for instance,  $\omega_k$  is substituted by zero.

The equation of the mechanical subsystem is

$$\tau_m \frac{d\omega}{d\tau} = T_e - T_L \quad (8)$$

where  $\tau_m$  is the mechanical time constant,  $\omega$  is the angular mechanical velocity of the rotor,  $T_e$  is the electromagnetic torque, and  $T_L$  is the load torque.  $T_e$  is computed from the  $z$  component of the vector product of two state variables, for instance, as

$$T_e = \boldsymbol{\psi}_s \times \mathbf{i}_s|_z = \psi_{s\alpha} i_{s\beta} - \psi_{s\beta} i_{s\alpha} \quad (9)$$

when  $\boldsymbol{\psi}_s = \psi_{s\alpha} + j\psi_{s\beta}$  and  $\mathbf{i}_s = i_{s\alpha} + j i_{s\beta}$  are the selected state variables, expressed by their components in stationary coordinates.

### C. Stator Current and Rotor Flux as the Selected State Variables

Most drive systems have a current control loop incorporated in their control structure. It is therefore advantageous to select the stator current vector as one state variable. The second state variable is then either the stator flux or the rotor flux linkage vector, depending on the problem at hand. Selecting the rotor current vector as a state variable is not very practical, since the rotor currents cannot be measured in a squirrel cage rotor.

Synchronous coordinates are chosen to represent the machine equations,  $\omega_k = \omega_s$ . Selecting the stator current and the rotor flux linkage vectors as state variables leads to the following system equations, obtained from (4) to (7):

$$\tau'_\sigma \frac{d\mathbf{i}_s}{d\tau} + \mathbf{i}_s = -j\omega_s \tau'_\sigma \mathbf{i}_s - \frac{k_r}{r_\sigma \tau_r} (j\omega \tau_r - 1) \boldsymbol{\psi}_r + \frac{1}{r_\sigma} \mathbf{u}_s \quad (10a)$$

$$\tau_r \frac{d\boldsymbol{\psi}_r}{d\tau} + \boldsymbol{\psi}_r = -j(\omega_s - \omega) \tau_r \boldsymbol{\psi}_r + l_m \mathbf{i}_s. \quad (10b)$$

The coefficients in (10) are the transient stator time constant  $\tau'_\sigma = \sigma l_s / r_\sigma$  and the rotor time constant  $\tau_r = l_r / r_r$ , where  $\sigma l_s$  is the total leakage inductance,  $\sigma = 1 - l_m^2 / l_s l_r$  is the total leakage factor,  $r_\sigma = r_s + k_r^2 r_r$  is an equivalent resistance, and  $k_r = l_m / l_r$  is the coupling factor of the rotor.

The selected coordinate system rotates at the electrical angular stator velocity  $\omega_s$  of the stator, and hence in synchronism with the revolving flux density and current density waves in the steady state. All space vectors will therefore assume a fixed position in this reference frame as long as the steady-state prevails.

The graphic interpretation of (8)–(10) is the signal flow diagram Fig. 5. This graph exhibits two fundamental winding

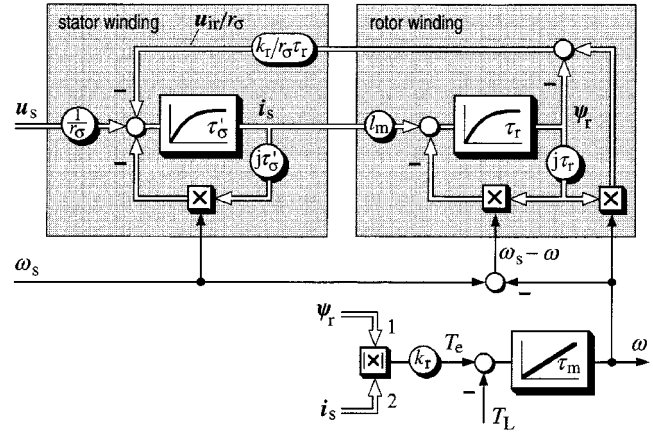


Fig. 5. Induction motor signal flow graph; state variables: stator current vector, rotor flux vector; representation in synchronous coordinates.

structures in its upper portion, representing the winding systems in the stator and the rotor, and their mutual magnetic coupling. Such fundamental structures are typical for any ac machine winding. The properties of such structure shall be explained with reference to the model of the stator winding in the upper left of Fig. 5. Here, the time constant of the first-order delay element is  $\tau'_\sigma$ . The same time constant reappears as factor  $j\tau'_\sigma$  in the local feedback path around the first-order delay element such that the respective state variable, here  $\mathbf{i}_s$ , gets multiplied by  $j\omega_s \tau'_\sigma$ . The resulting signal  $j\omega_s \tau'_\sigma \mathbf{i}_s$ , if multiplied by  $r_\sigma$ , is the motion-induced voltage that is generated by the rotation of the winding with respect to the selected reference frame. While the factor  $\omega_s$  represents the angular velocity of the rotation, the sign of the local feedback signal, which is minus in this example, indicates the direction of rotation: the stator winding rotates counterclockwise at  $\omega_s$  in a synchronous reference frame.

The stator winding is characterized by the small transient time constant  $\tau'_\sigma$ , being determined by the leakage inductances and the winding resistances both in the stator and the rotor. The dynamics of the rotor flux are governed by the larger rotor time constant  $\tau_r$  if the rotor is excited by the stator current vector  $\mathbf{i}_s$  (see Fig. 5). The rotor flux reacts on the stator winding through the rotor-induced voltage

$$\mathbf{u}_{ir} = \frac{k_r}{\tau_r} (j\omega \tau_r - 1) \boldsymbol{\psi}_r \quad (11)$$

in which the component  $j\omega \boldsymbol{\psi}_r$  predominates over  $\boldsymbol{\psi}_r / \tau_r$  unless the speed is very low. A typical value of the normalized rotor time constant is  $\tau_r = 80$ , equivalent to 250 ms, while  $\boldsymbol{\psi}_r$  is close to unity in the base speed range.

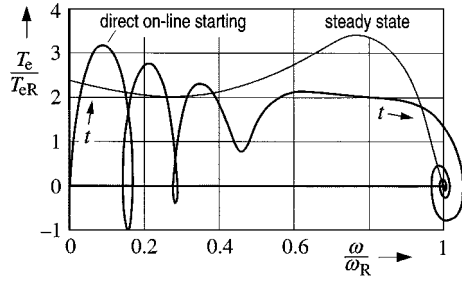
The electromagnetic torque as the input signal to the mechanical subsystem is expressed by the selected state variables and derived from (6), (7), and (9) as

$$T_e = k_r \cdot \boldsymbol{\psi}_r \times \mathbf{i}_s|_z. \quad (12)$$

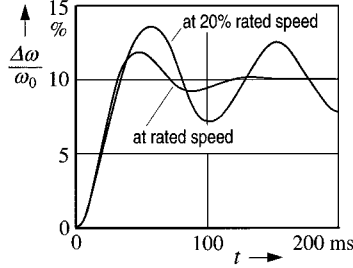
### D. Speed Estimation at Very Low Stator Frequency

The dynamic model of the induction motor is used to investigate the special case of operation at very low stator frequency,  $\omega_s \rightarrow 0$ . The stator reference frame is used for this





(a)



(b)

**Fig. 7.** Dynamic behavior of the uncontrolled induction motor. (a) Large-signal response: direct on-line starting compared with the steady-state characteristic. (b) Small-signal response: speed oscillations following a step change of the stator frequency.

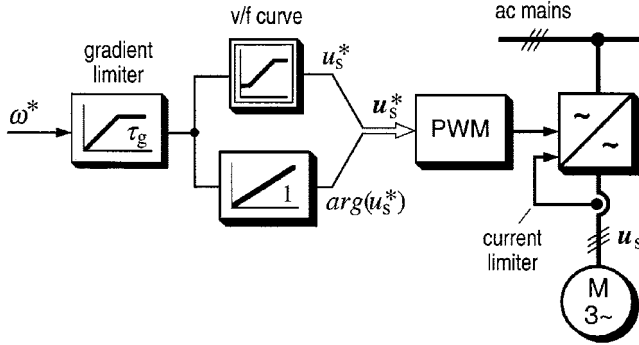


**Fig. 8.** Constant V/Hz control.

### III. CONSTANT V/Hz CONTROL

#### A. Low Cost and Robust Drives

One way of dealing with the complex and nonlinear dynamics of induction machines in adjustable speed drives is avoiding excitation at their eigenfrequencies. To this aim, a gradient limiter reduces the bandwidth of the stator frequency command signal as shown in Fig. 8. The band-limited stator frequency signal then generates the stator voltage reference magnitude  $u_s^*$  while its integral determines the phase angle  $\arg(u_s^*)$ .

The  $v/f$  characteristic in Fig. 8 is derived from (4), neglecting the resistive stator voltage drop  $r_s \mathbf{i}_s$  and, in view of band-limited excitation, assuming steady-state operation,  $d\psi_s/dt \approx 0$ . This yields

$$\mathbf{u}_s = j\omega_s \psi_s \quad (16)$$

or  $u_s/\omega_s = \text{const.}$  (or  $v/f = \text{const.}$ ) when the stator flux is maintained at its nominal value in the base speed range. Field weakening is obtained by maintaining  $u_s = u_{s \max} = \text{const.}$  while increasing the stator frequency beyond its nom-

inal value. At very low stator frequency is a preset minimum value of the stator voltage programmed to account for the resistive stator voltage drop.

The signals  $u_s^*$  and  $\arg(u_s^*)$  thus obtained constitute the reference vector  $\mathbf{u}_s^*$  of the stator voltage, which in turn controls a pulsewidth modulator (PWM) to generate the switching sequence of the inverter. Overload protection is achieved by simply inhibiting the firing signals of the semiconductor devices if the machine currents exceed a permitted maximum value.

Since  $v/f$ -controlled drives operate purely as feedforward systems, the mechanical speed  $\omega$  differs from the reference speed  $\omega_s^*$  when the machine is loaded. The difference is the slip frequency, equal to the electrical frequency  $\omega_r$  of the rotor currents. The maximum speed error is determined by the nominal slip, which is 3%–5% of nominal speed for low-power machines and less at higher power. A load current-dependent slip compensation scheme can be employed to reduce the speed error [6].

Constant V/Hz control ensures robustness at the expense of reduced dynamic performance, which is adequate for applications like pump and fan drives and tolerable for other applications if cost is an issue. A typical value for torque rise time is 100 ms. The absence of closed-loop control and the restriction to low dynamic performance make  $v/f$ -controlled drives very robust. They exhibit stable operation even in the critical low-speed range where vector control fails to maintain stability (Section VII-A). Also, for very high-speed applications like centrifuges and grinders, open-loop control is an advantage: The current control system of closed-loop schemes tends to destabilize when operated at field weakening up to 5–10 times the nominal frequency of 50 or 60 Hz. The amplitude of the motion-induced voltage  $j\omega_s \tau'_\sigma \mathbf{i}_s$  in the stator (Fig. 5) becomes very high at those high values of the stator frequency  $\omega_s$ . Here, the complex coefficient  $j\omega_s$  introduces an undesired voltage component in quadrature to any manipulated change of the stator voltage vector that the current controllers command. The phase displacement in the motion-induced voltage impairs the stability.

The particular attraction of  $v/f$ -controlled drives is their extremely simple control structure which favors an implementation by a few highly integrated electronic components. These cost-saving aspects are specifically important for applications at low power below 5 kW. At higher power, the power components themselves dominate the system cost, permitting the implementation of more sophisticated control methods. These serve to overcome the major disadvantage of  $v/f$  control: the reduced dynamic performance. Even so, the cost advantage makes  $v/f$  control very attractive for low-power applications, while their robustness favors its use at high power when a fast response is not required. In total, such systems contribute a substantial share of the market for sensorless ac drives.

#### B. Drives for Moderate Dynamic Performance

An improved dynamic performance of  $v/f$ -controlled drives can be achieved by an adequate design of the control structure. The signal flow graph Fig. 9 gives an example [7].

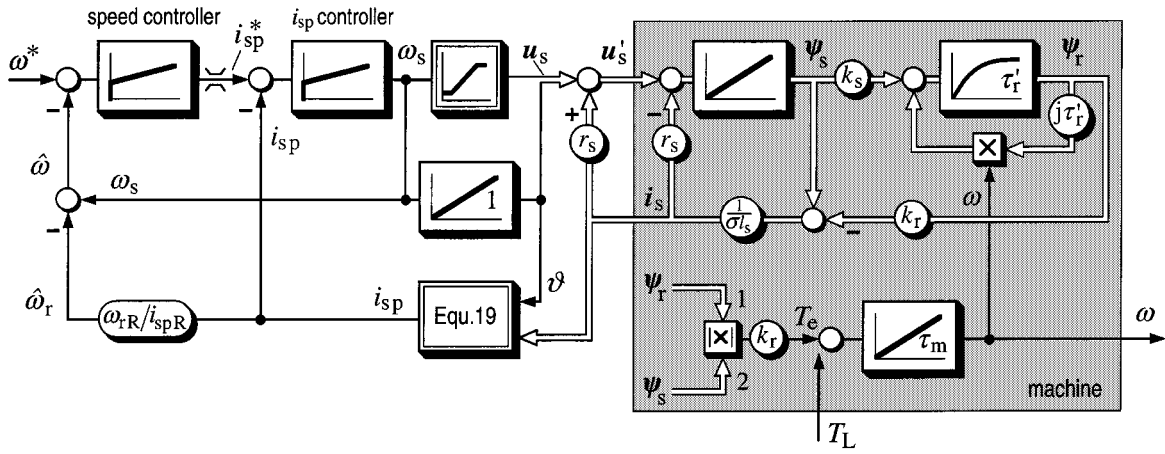


Fig. 9. Drive control system for moderate dynamic requirements.

The machine dynamics are represented here in terms of the state variables  $\psi_s$  and  $\psi_r$ . The system equations are derived in the stationary reference frame, letting  $\omega_k = 0$  in (4)–(7). The result is

$$\frac{d\psi_s}{d\tau} = \mathbf{u}_s - r_s \frac{1}{\sigma l_s} (\psi_s - k_r \psi_r) \quad (17a)$$

$$\tau_r' \frac{d\psi_r}{d\tau} + \psi_r = j\omega \tau_r' \psi_r + k_s \psi_s \quad (17b)$$

where  $\tau_r' = \sigma \tau_r = \sigma l_r / r_r$  is a transient rotor time constant and  $k_s$  is the coupling factor of the stator. The corresponding signal flow graph of the machine model is highlighted by the shaded area on the right-hand side of Fig. 9. The graph shows that the stator flux vector is generated as the integral of  $\mathbf{u}_s - r_s \cdot \mathbf{i}_s$ , where

$$\mathbf{i}_s = \frac{1}{\sigma l_s} (\psi_s - k_r \psi_r). \quad (18)$$

The normalized time constant of the integrator is unity.

The key quantity of this control concept is the active stator current  $i_{sp}$ , computed in stationary coordinates as

$$i_{sp} = \frac{\mathbf{u}_s^* \circ \mathbf{i}_s}{u_s^*} = i_{s\alpha} \cos \vartheta + i_{s\beta} \sin \vartheta \quad (19)$$

from the measured orthogonal stator current components  $i_{s\alpha}$  and  $i_{s\beta}$  in stationary coordinates, where  $\mathbf{i}_s = i_{s\alpha} + j i_{s\beta}$  and  $\vartheta$  is the phase angle of the stator voltage reference vector  $\mathbf{u}_s^* = u_s^* \cdot e^{j\vartheta}$ , a control input variable. The active stator current  $i_{sp}$  is proportional to the torque. Accordingly, its reference value  $i_{sp}^*$  is generated as the output of the speed controller. Speed estimation is based on the stator frequency signal  $\omega_s$  as obtained from the  $i_{sp}$ -controller, and on the active stator current  $i_{sp}$ , which is proportional the rotor frequency. The nominal value  $i_{spR}$  of the active stator current produces nominal slip at rotor frequency  $\omega_{rR}$ , thus  $\hat{\omega}_r = \omega_{rR} / i_{spR} \cdot i_{sp}$ . The estimated speed is then

$$\hat{\omega} = \omega_s - \hat{\omega}_r \quad (20)$$

where the hatch marks  $\hat{\omega}_r$  as an estimated variable.

An inner loop controls the active stator current  $i_{sp}$ , with its reference signal limited to prevent overloading the inverter and to avoid pull-out of the induction machine if the load torque is excessive.

Fig. 9 shows that an external  $r_s \cdot \mathbf{i}_s$ -signal compensates and eliminates the internal resistive voltage drop of the machine. This makes the trajectory of the stator flux vector independent of the stator current and the load. It provides a favorable dynamic behavior of the drive system and eliminates the need for the conventional acceleration limiter (Fig. 8) in the speed reference channel. A torque rise time around 10 ms can be achieved [7], which matches the dynamic performance of a thyristor converter controlled dc drive.

#### IV. MACHINE MODELS

Machine models are used to estimate the motor shaft speed and, in high-performance drives with field-oriented control, to identify the time-varying angular position of the flux vector. In addition, the magnitude of the flux vector is estimated for field control.

Different machine models are employed for this purpose, depending on the problem at hand. A machine model is implemented in the controlling microprocessor by solving the differential equations of the machine in real time while using measured signals from the drive system as the forcing functions.

The accuracy of a model depends on the degree of coincidence that can be obtained between the model and the modeled system. Coincidence should prevail both in terms of structures and parameters. While the existing analysis methods permit establishing appropriate model structures for induction machines, the parameters of such model are not always in good agreement with the corresponding machine data. Parameters may significantly change with temperature or with the operating point of the machine. On the other hand, the sensitivity of a model to parameter mismatch may differ, depending on the respective parameter, and the particular variable that is estimated by the model.

Differential equations and signal flow graphs are used in this paper to represent the dynamics of an induction motor and its various models used for state estimation. The characterizing parameters represent exact values when describing the machine itself; they represent estimated values for machine models. For better legibility, the model parameters are mostly not specifically marked ( $\hat{\cdot}$ ) as estimated values.



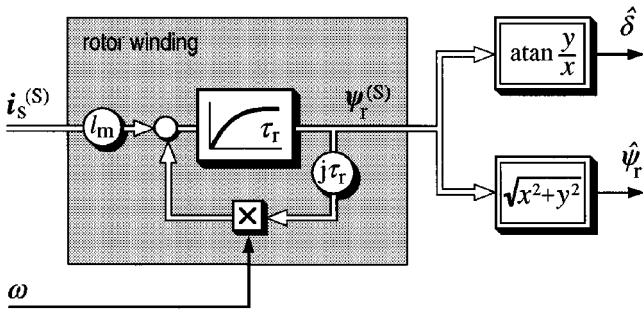


Fig. 10. Rotor model in stator coordinates.

Suitable models for field angle estimation are the model of the stator winding (see Fig. 11) and the model of the rotor winding shown in Fig. 10. Each model has its merits and drawbacks.

#### A. The Rotor Model

The rotor model is derived from the differential equation of the rotor winding. It can be either implemented in stator coordinates or in field coordinates. The rotor model in stator coordinates is obtained from (10b) in a straightforward manner by letting  $\omega_s = 0$  to obtain

$$\tau_r \frac{d\psi_r}{dt} + \psi_r = j\omega\tau_r\psi_r + l_m i_s. \quad (21)$$

Fig. 10 shows the signal flow graph. The measured values of the stator current vector  $i_s$  and of the rotational speed  $\omega$  are the input signals to the model. The output signal is the rotor flux linkage vector  $\psi_r^{(S)}$ , marked by the superscript (S) as being referred to in stator coordinates. The argument  $\arg(\psi_r)$  of the rotor flux linkage vector is the rotor field angle  $\delta$ . The magnitude  $\psi_r$  is required as a feedback signal for flux control. The two signals are obtained as the solution of

$$\psi_r^{(S)} = \psi_r \cos \delta + j\psi_r \sin \delta = \psi_{r\alpha} + j\psi_{r\beta} \quad (22)$$

where the subscripts  $\alpha$  and  $\beta$  mark the respective components in stator coordinates. The result is

$$\delta = \arctan \frac{\psi_{r\beta}}{\psi_{r\alpha}}, \quad \psi_r = \sqrt{\psi_{r\alpha}^2 + \psi_{r\beta}^2}. \quad (23)$$

The rotor field angle  $\delta$  marks the angular orientation of the rotor flux vector. It is always referred to in stator coordinates.

The functions (23) are modeled at the output of the signal flow graph Fig. 10. In a practical implementation, these functions can be condensed into two numeric tables that are read from the microcontroller program.

The accuracy of the rotor model depends on the correct setting of the model parameters in (21). It is particularly rotor time constant  $\tau_r$  that determines the accuracy of the estimated field angle, the most critical variable in a vector-controlled drive. The other model parameter is the mutual inductance  $l_m$ . It acts as a gain factor as seen in Fig. 10 and does not affect the field angle. It does have an influence on the magnitude of the flux linkage vector, which is less critical.

#### B. The Stator Model

The stator model is used to estimate the stator flux linkage vector or the rotor flux linkage vector, without requiring a speed signal. It is therefore a preferred machine model for

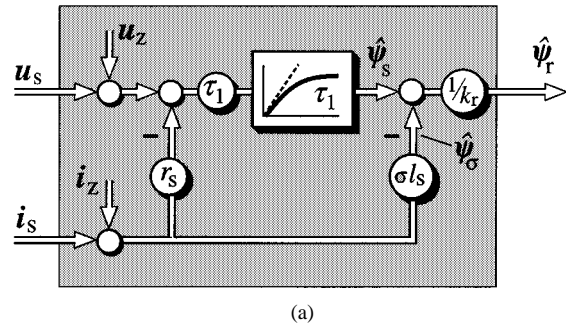


Fig. 11. Stator model in stationary coordinates; the ideal integrator is substituted by a low-pass filter. (a) Signal flow graph. (b) Bode diagram.

sensorless speed control applications. The stator model is derived by integrating the stator voltage equation (4) in stator coordinates,  $\omega_k = 0$ , from which

$$\psi_s = \int (\mathbf{u}_s - r_s \mathbf{i}_s) d\tau \quad (24)$$

is obtained. Equations (6) and (7) are used to determine the rotor flux linkage vector from (24) to yield

$$\psi_r = \frac{1}{k_r} \left( \int (\mathbf{u}_s - r_s \mathbf{i}_s) d\tau - \sigma l_s \mathbf{i}_s \right) = \frac{1}{k_r} (\psi_s - \psi_\sigma). \quad (25)$$

The equation shows that the rotor flux linkage is basically the difference between the stator flux linkage and the leakage flux  $\psi_\sigma$ .

One of the two model equations (24) or (25) can be used to estimate the respective flux linkage vector, from which the pertaining field angle and the magnitude of the flux linkage are obtained. The signal flow diagram Fig. 11(a) illustrates rotor flux estimation according to (25).

The stator model (24) or (25) is difficult to apply in practice since an error in the acquired signals  $\mathbf{u}_s$  and  $\mathbf{i}_s$  and offset and drift effects in the integrating hardware will accumulate as there is no feedback from the integrator output to its input. All these disturbances, which are generally unknown, are represented by two disturbance vectors  $\mathbf{u}_z(\tau)$  and  $\mathbf{i}_z(\tau)$  in Fig. 11(a). The resulting runaway of the output signal is a fundamental problem of an open integration. A negative, low-gain feedback is therefore added which stabilizes the integrator and prevents its output from increasing without bounds. The feedback signal converts the integrator into a

first order delay having a low corner frequency  $1/\tau_1$ , and the stator models (24) and (25) become

$$\tau_1 \frac{d\psi_s}{d\tau} + \psi_s = \tau_1 (\mathbf{u}_s - r_s \mathbf{i}_s), \quad \psi_r = \frac{1}{k_r} (\psi_s - \sigma l_s \mathbf{i}_s) \quad (26)$$

and

$$\tau_1 \frac{d\psi_r}{d\tau} + \psi_r = \frac{\tau_1}{k_r} \left( \mathbf{u}_s - r_s \mathbf{i}_s - \sigma l_s \frac{d\mathbf{i}_s}{d\tau} \right) \quad (27)$$

respectively.

The Bode diagram [Fig. 11(b)] shows that the first-order delay, or low-pass filter, behaves as an integrator for frequencies much higher than the corner frequency. It is obvious that the model becomes inaccurate when the frequency reduces to values around the corner frequency. The gain is then reduced and, more importantly, the  $90^\circ$  phase shift of the integrator is lost. This causes an increasing error in the estimated field angle as the stator frequency reduces.

The decisive parameter of the stator model is the stator resistance  $r_s$ . The resistance of the winding material increases with temperature and can vary in a 1 : 2 range. A parameter error in  $r_s$  affects the signal  $r_s \mathbf{i}_s$  in Fig. 11. This signal dominates the integrator input when the magnitude of  $\mathbf{u}_s$  reduces at low speed. Reversely, it has little effect on the integrator input at higher speed as the nominal value of  $r_s \mathbf{i}_s$  is low. The value ranges between 0.02–0.05 p.u., where the lower values apply to high-power machines.

To summarize, the stator model is sufficiently robust and accurate at higher stator frequency. Two basic deficiencies let this model degrade as the speed reduces: the integration problem and the sensitivity of the model to stator resistance mismatch. Depending on the accuracy that can be achieved in a practical implementation, the lower limit of stable operation is reached when the stator frequency is around 1–3 Hz.

## V. ROTOR FIELD ORIENTATION

Control with field orientation, also referred to as vector control, implicates processing the current signals in a specific synchronous coordinate system. Rotor field orientation uses a reference frame aligned with the rotor flux linkage vector. It is one of the two basic subcategories of vector control shown in Fig. 1.

### A. Principle of Rotor Field Orientation

A fast current control system is usually employed to force the stator MMF distribution to a desired location and intensity in space, independent of the machine dynamics. The current signals are time-varying when processed in stator coordinates. The control system then produces an undesirable velocity error even in the steady state. It is therefore preferred to implement the current control in synchronous coordinates. All system variables then assume constant values at steady state, and zero steady-state error can be achieved.

The bandwidth of the current control system is basically determined by the transient stator time constant  $\tau'_s$ , unless the switching frequency of the PWM inverter is lower than about 1 kHz. The other two time constants of the machine (Fig. 5), the rotor time constant  $\tau_r$  and the mechanical time

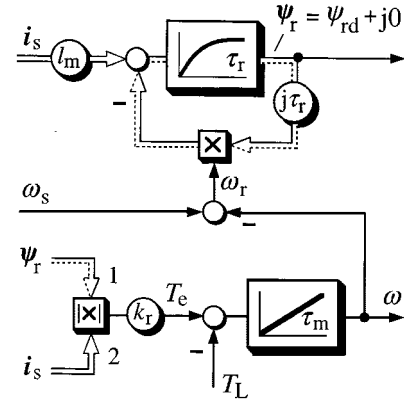


Fig. 12. Induction motor signal flow graph at forced stator currents. The dotted lines represent zero signals at rotor field orientation.

constant  $\tau_m$ , are much larger in comparison. The current control therefore rejects all disturbances that the dynamic eigen-behavior of the machine might produce, thus eliminating the influence of the stator dynamics. The dynamic order reduces in consequence, the system only being characterized by the complex rotor equation (10b) and the scalar equation (8) of the mechanical subsystem. Equations (10b) and (8) form a second-order system. Referring to synchronous coordinates,  $\omega_k = \omega_s$ , the rotor equation (10b) is rewritten as

$$\tau_r \frac{d\psi_r}{d\tau} + \psi_r = -j\omega_r \tau_r \psi_r + l_m \mathbf{i}_s \quad (28)$$

where  $\omega_r$  is the angular frequency of the induced rotor voltages. The resulting signal flow graph (Fig. 12) shows that the stator current vector acts as an independent forcing function on the residual dynamic system. Its value is commanded by the complex reference signal  $\mathbf{i}_s^*$  of the current control loop.

To achieve dynamically decoupled control of the now decisive system variables  $T_e$  and  $\psi_r$ , a particular synchronous coordinate system is defined, having its real axis aligned with the rotor flux vector [8]. This reference frame is the rotor field oriented  $dq$ -coordinate system. Here, the imaginary rotor flux component, or  $q$ -component  $\psi_{rq}$ , is zero by definition, and the signals marked by dotted lines in Fig. 12 assume zero values.

To establish rotor field orientation, the  $q$  component of the rotor flux vector must be forced to zero. Hence, the  $q$ -component of the input signal to the  $\tau_r$  delay in Fig. 12 must be also zero. The balance at the input summing point of the  $\tau_r$  delay thus defines the condition for rotor field orientation

$$l_m i_q = \omega_r \tau_r \psi_{rd} \quad (29)$$

which is put into effect by adjusting  $\omega_r$  appropriately. If condition (29) is enforced, the signal flow diagram of the motor assumes the familiar dynamic structure of a dc machine (Fig. 13). The electromagnetic torque  $T_e$  is now proportional to the forced value of the  $q$ -axis current  $i_q$  and, hence, is independently controllable. Also, the rotor flux is independently controlled by the  $d$ -axis current  $i_d$ , which is kept at its nominal, constant value in the base speed range. The machine dynamics are therefore reduced to the dynamics of the mechanical subsystem which is of first

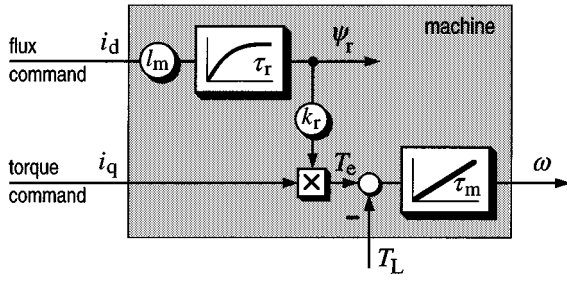


**Fig. 13.** Signal flow graph of the induction motor at rotor field orientation.

order. The control concept also eliminates the nonlinearities of the system and inhibits its inherent tendency to oscillate during transients, illustrated in Fig. 7.

### B. Model Reference Adaptive System Based on the Rotor Flux

The model reference approach (MRAS) makes use of the redundancy of two machine models of different structures that estimate the same state variable on the basis of different sets of input variables [9]. Both models are referred to in the stationary reference frame. The stator model (26) in the upper portion of Fig. 14 serves as a reference model. Its output is the estimated rotor flux vector  $\hat{\psi}_r^S$ . The superscript *S* indicates that  $\hat{\psi}_r^S$  originates from the stator model.

The rotor model is derived from (10b), where  $\omega_s$  is set to zero for stator coordinates

$$\tau_r \frac{d\psi_r}{dt} + \psi_r = j\omega\tau_r\psi_r + l_m i_s. \quad (30)$$

This model estimates the rotor flux from the measured stator current and from a tuning signal  $\hat{\omega}$  in Fig. 14. The tuning signal is obtained through a proportional-integral (PI) controller from a scalar error signal  $e = \hat{\psi}_r^S \times \hat{\psi}_r^R|_z = \hat{\psi}_r^S \hat{\psi}_r^R \sin \alpha$ , which is proportional to the angular displacement  $\alpha$  between the two estimated flux vectors. As the error signal  $e$  gets minimized by the PI controller, the tuning signal  $\hat{\omega}$  approaches the actual speed of the motor. The rotor model as the adjustable model then aligns its output vector  $\hat{\psi}_r^R$  with the output vector  $\hat{\psi}_r^S$  of the reference model.

The accuracy and drift problems at low speed, inherent to the open integration in the reference model, are alleviated by using a delay element instead of an integrator in the stator model in Fig. 14. This eliminates an accumulation of the drift error. **It also makes the integration ineffective in the frequency range around and below  $1/\tau_1$  and necessitates the addition of an equivalent bandwidth limiter in the input of the adjustable rotor model.** Below the cutoff frequency  $\omega_{sR}/\tau_1 \approx 1\text{--}3$  Hz, speed estimation becomes necessarily inaccurate. A reversal of speed through zero in the course of a transient process is nevertheless possible, if such process is fast enough not to permit the output of the  $\tau_1$ -delay element to assume erroneous values. However, if the drive is operated close to zero stator frequency for a longer period of time, the estimated flux goes astray and speed estimation is lost.

The speed control system superimposed to the speed estimator is shown in Fig. 15. The estimated speed signal  $\hat{\omega}$  is supplied by the model reference adaptive system Fig. 14. The

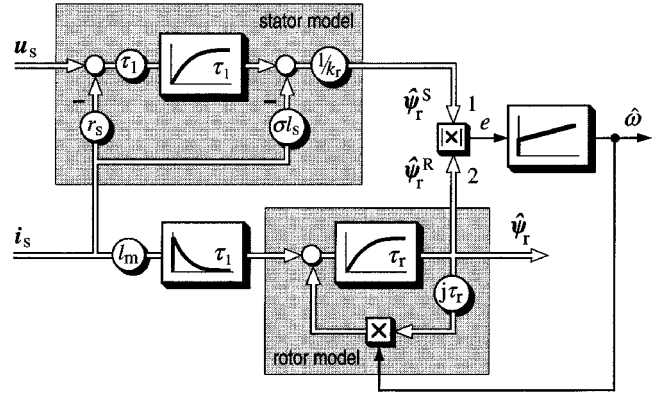


**Fig. 14.** Model reference adaptive system for speed estimation; reference variable: rotor flux vector.

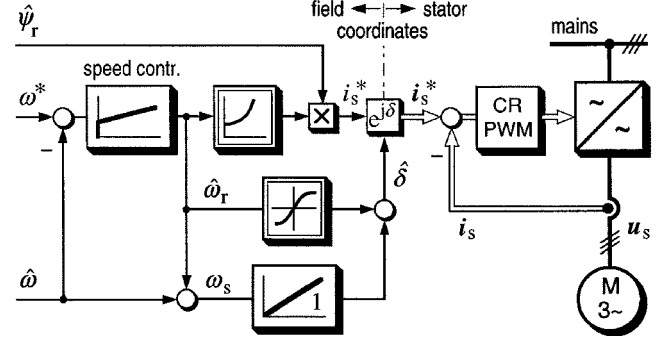


**Fig. 15.** Speed and current control system for MRAS estimators. CR PWM: current regulated PWM.

speed controller in Fig. 15 generates a rotor frequency signal  $\hat{\omega}_r$ , which controls the stator current magnitude

$$i_s = \frac{\hat{\psi}_r}{l_s} \sqrt{1 + \hat{\omega}_r^2 \tau_r^2} \quad (31)$$

and the current phase angle

$$\delta = \int \hat{\omega}_s d\tau + \arctan(\hat{\omega}_r \tau_r). \quad (32)$$

Equations (31) and (32) are derived from (29) and from the steady-state solution  $i_d = \psi_r/l_m$  of (21) in field coordinates, where  $\psi_{rq} \approx 0$  and, hence,  $\psi_{rd} = \psi_r$  is assumed since field orientation exists.

It is a particular asset of this approach that the accurate orientation of the injected current vector is maintained even if the model value of  $\tau_r$  differs from the actual rotor time constant of the machine. The reason is that the same, even erroneous value of  $\tau_r$  is used both in the rotor model and in the control algorithm (31) and (32) of the speed control scheme of Fig. 15. If the tuning controller in Fig. 14 maintains zero error, the control scheme exactly replicates the same dynamic relationship between the stator current vector and the rotor flux vector that exists in the actual motor, even in the presence of a rotor time constant error [9]. However, the accuracy of speed estimation, reflected in the feedback signal  $\hat{\omega}$  to the speed controller, does depend on the error in  $\tau_r$ . The speed error may be even higher than with those methods that estimate the rotor frequency  $\omega_r$  and use (20) to compute the speed:  $\hat{\omega} = \omega_s - \hat{\omega}_r$ . The reason is that the stator frequency  $\omega_s$  is a control input to the system and therefore accurately



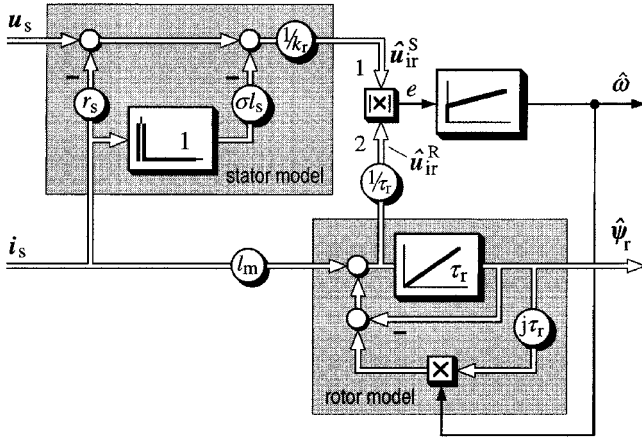


**Fig. 16.** Model reference adaptive system for speed estimation; reference variable: rotor-induced voltage.

known. Even if  $\hat{\omega}_r$  in (20) is erroneous, its nominal contribution to  $\hat{\omega}$  is small (2%–5% of  $\omega_{sR}$ ). Thus, an error in  $\hat{\omega}_r$  does not affect  $\hat{\omega}$  very much, unless the speed is very low.

A more severe source of inaccuracy is a possible mismatch of the reference model parameters, particularly of the stator resistance  $r_s$ . Good dynamic performance of the system is reported by Schauder above 2-Hz stator frequency [9].

### C. Model Reference Adaptive System Based on the Induced Voltage

The model reference adaptive approach, if based on the rotor-induced voltage vector rather than the rotor flux linkage vector, offers an alternative to avoid the problems involved with open integration [10]. In stator coordinates, the rotor-induced voltage is the derivative of the rotor flux linkage vector. Hence, differentiating (25) yields

$$\frac{d\psi_r}{d\tau} = \frac{1}{k_r} \left( u_s - r_s i_s - \sigma l_s \frac{di_s}{d\tau} \right) \quad (33)$$

which is a quantity that provides information on the rotor flux vector from the terminal voltage and current, without the need to perform an integration. Using (33) as the reference model leaves (21) as

$$\tau_r \frac{d\psi_r}{d\tau} = -\psi_r + j\omega_{\tau} \psi_r + l_m i_s \quad (34)$$

to define the corresponding adjustable model. The signal flow graph of the complete system is shown in Fig. 16.

The open integration is circumvented in this approach and, other than in the MRAC system based on the rotor flux, there are no low-pass filters that create a bandwidth limit. However, the derivative of the stator current vector must be computed to evaluate (33). If the switching harmonics are processed as part of  $u_s$ , these must be also contained in  $i_s$  (and in  $di_s/d\tau$  as well) as the harmonic components must cancel on the right-hand side of (33).

### D. Feedforward Control of Stator Voltages

In the approach of Okuyama *et al.* [11], the stator voltages are derived from a steady-state machine model and used as the basic reference signals to control the machine. Therefore, through its model, it is the machine itself that lets the inverter

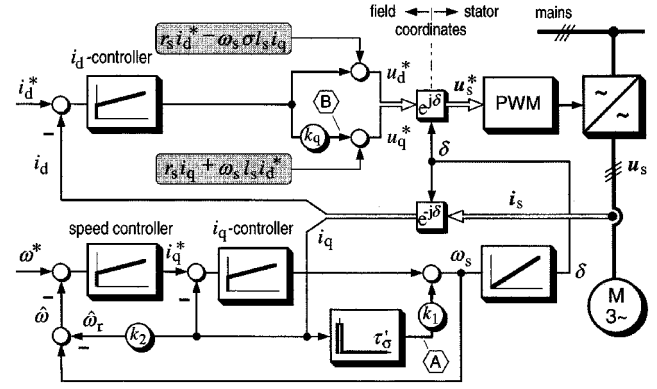


**Fig. 17.** Feedforward control of stator voltages, rotor flux orientation;  $k_1 = r_s \psi_{rd0} / k_r$ ,  $k_2 = l_m / \tau_r \psi_{rd0}$ .

duplicate the voltages which prevail at its terminals in a given operating point. This process can be characterized as self-control.

The components of the voltage reference signal are derived in field coordinates from (10) under the assumption of steady-state conditions,  $d/d\tau \approx 0$ , from which  $\psi_{rd} = l_m i_{sd}$  follows, and using the approximation  $\omega \approx \omega_s$  as follows:

$$u_d = r_s i_d - \omega_s \sigma l_s i_q \quad (35a)$$

$$u_q = r_s i_q + \omega_s l_s i_d. \quad (35b)$$

The  $d$ -axis current  $i_d$  is replaced by its reference value  $i_d^*$ . The resulting feedforward signals are represented by the equations marked by the shaded frames in Fig. 17. The signals depend on machine parameters, which creates the need for error compensation by superimposed control loops. An  $i_d$ -controller ensures primarily the error correction of  $u_d$ , thus governing the machine flux. The signal  $i_q^*$ , which represents the torque reference, is obtained as the output of the speed controller. The estimated speed  $\hat{\omega}$  is computed from (20) as the difference of the stator frequency  $\omega_s$  and the estimated rotor frequency  $\hat{\omega}_r$ ; the latter is proportional to, and therefore derived from, the torque producing current  $i_q$ . Since the torque increases when the velocity of the revolving field increases,  $\omega_s$  and, in consequence, the field angle  $\delta$  can be derived from the  $i_q$  controller.

Although the system thus described is equipped with controllers for both stator current components  $i_d$  and  $i_q$ , the internal cross-coupling between the input variables and the state variables of the machine is not eliminated under dynamic conditions; the desired decoupled machine structure of Fig. 13 is not established. The reason is that the position of the rotating reference frame, defined by the field angle  $\delta$ , is not determined by the rotor flux vector  $\psi_r$ . It is governed by the  $q$ -current error instead, which, through the  $i_q$ -controller, accelerates or decelerates the reference frame.

To investigate the situation, the dynamic behavior of the machine is modeled using the signal flow graph of Fig. 5. Only small deviations from a state of correct field orientation and correct flux magnitude control are considered. A reduced signal flow graph in Fig. 18 is thereby obtained in which the  $d$ -axis rotor flux is considered constant, denoted as  $\psi_{rd0}$ . A nonzero value of the  $q$ -axis rotor flux  $\psi_{rq}$  indicates a



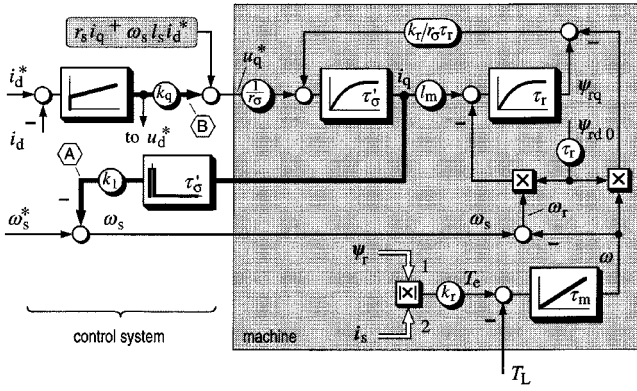


**Fig. 18.** Compensation channels (thick lines at A and B) for the sensorless speed control system in Fig. 17;  $k_1 = 1/k_r r_\sigma \psi_{rd0}$ .

misalignment of the field-oriented reference frame. It is now assumed that the mechanical speed  $\omega$  changes by a sudden increase of the load torque  $T_L$ . The subsequent decrease of  $\omega$  increases  $\omega_r$  and hence produces a negative  $d\psi_{rq}/d\tau$  at signal the input of the  $\tau_r$ -delay. Simultaneously, the  $q$ -axis component  $-k_r/r_\sigma \cdot \omega\psi_{rd0}$  of the rotor-induced voltage is increased, which is the back-EMF that acts on the stator. The consequence is that  $i_q$  rises, delayed by the transient stator time constant  $\tau'_\sigma$ , which restores  $d\psi_{rq}/d\tau$  to its original zero value after the delay. Before this readjustment takes place, though,  $\psi_{rq}$  has already assumed a permanent nonzero value, and field orientation is lost.

A similar effect occurs on a change of  $\omega_s^*$  which instantaneously affects  $d\psi_{rq}/d\tau$ , while this disturbance is compensated only after a delay of  $\tau'_\sigma$  by the feedforward adjustment of  $u_q^*$  through  $\omega_s$ .

Both undesired perturbations are eliminated by the addition of a signal proportional to  $-di_q/d\tau$  to the stator frequency input of the machine controller. This compensation channel is marked A in Figs. 17 and 18.

Still, the mechanism of maintaining field orientation needs further improvement. In the dynamic structure of Fig. 5, the signal  $-j\omega_r\psi_r$ , which essentially contributes to back-EMF vector, influences the stator current derivative. A misalignment between the reference frame and the rotor flux vector produces a nonzero  $\psi_{rq}$  value, giving rise to a back-EMF component that changes  $i_d$ . Since the feedforward control of  $u_d^*$  is determined by (35a) on the assumption of existing field alignment, such a deviation will invoke a correcting signal from the  $i_d$  controller. This signal is used to influence, through a gain constant  $k_q$ , upon the quadrature voltage  $u_q^*$  (channel B in Figs. 17 and 18) and hence on  $i_q$  as well, causing the  $i_q$  controller to accelerate or decelerate the reference frame to reestablish accurate field alignment.

Torque rise time of this scheme is reported around 15 ms; speed accuracy is within  $\pm 1\%$  above 3% rated speed and  $\pm 12$  rpm at 45 rpm [11].

#### E. Rotor Field Orientation With Improved Stator Model

A sensorless rotor field orientation scheme based on the stator model is described by Ohtani [12]. The upper portion of Fig. 19 shows the classical structure in which the

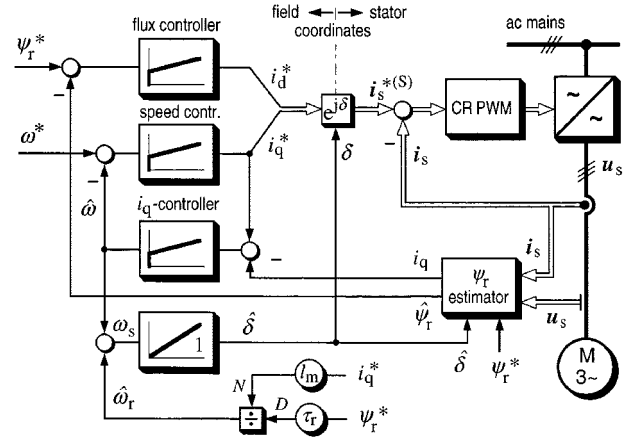


**Fig. 19.** Sensorless speed control based on direct  $i_q$  estimation and rotor field orientation. CRPWM: current regulated PWM;  $N$ : numerator,  $D$ : denominator.

controllers for speed and rotor flux generate the current reference vector  $\mathbf{i}_s^*$  in field coordinates. This signal is transformed to stator coordinates and processed by a set of fast current controllers. A possible misalignment of the reference frame is detected as the difference of the measured  $q$ -axis current from its reference value  $i_q^*$ . This error signal feeds a PI controller, the output of which is the estimated mechanical speed. It is added to an estimated value  $\hat{\omega}_r$  of the rotor frequency, obtained with reference to the condition for rotor field orientation (29), but computed from the reference values  $i_q^*$  and  $\psi_r^*$ . The reason is that the measured value  $i_q$  is contaminated by inverter harmonics, while the estimated rotor flux linkage vector  $\hat{\psi}_r$  is erroneous at low speed. The integration of  $\omega_s$  provides the field angle  $\delta$ .

The stator model is used to estimate the rotor flux vector  $\psi_r$ . The drift problems of an open integration at low frequency are avoided by a band-limited integration by means of a first-order delay. This entails a severe loss of gain in  $\psi_r$  at low stator frequency, while the estimated field angle lags considerably behind the actual position of the rotor field. The Bode plot in Fig. 11(b) demonstrates these effects.

An improvement is brought about by the following considerations. The transfer function of an integrator is

$$\tilde{\psi}_r = \frac{1}{s} \tilde{\mathbf{u}}_{ir} = \frac{1}{s} \tilde{\mathbf{u}}_{ir} \frac{\tau_1 s + 1}{\tau_1 s + 1} \quad (36)$$

where  $\tilde{\psi}_r$  and  $\tilde{\mathbf{u}}_{ir}$  are the Laplace transforms of the respective space vectors, and  $\mathbf{u}_{ir}$  is the rotor-induced voltage in the stator windings of (11). The term on the right-hand side is expanded by a fraction of unity value. This expression is then decomposed as

$$\tilde{\psi}_r = \frac{\tau_1}{\tau_1 s + 1} \tilde{\mathbf{u}}_{ir} + \frac{1}{\tau_1 s + 1} \cdot \frac{1}{s} \tilde{\mathbf{u}}_{ir} = \tilde{\psi}_{r1} + \tilde{\psi}_{r2}. \quad (37)$$

One can see from (36) that the factor  $\tilde{\mathbf{u}}_{ir}/s$  on the right-hand side equals the rotor flux vector  $\tilde{\psi}_r$ , which variable is now substituted by its reference value  $\tilde{\psi}_r^*$ .

$$\tilde{\psi}_r = \frac{\tau_1}{\tau_1 s + 1} \tilde{\mathbf{u}}_{ir} + \frac{1}{\tau_1 s + 1} \cdot \tilde{\psi}_r^*. \quad (38)$$

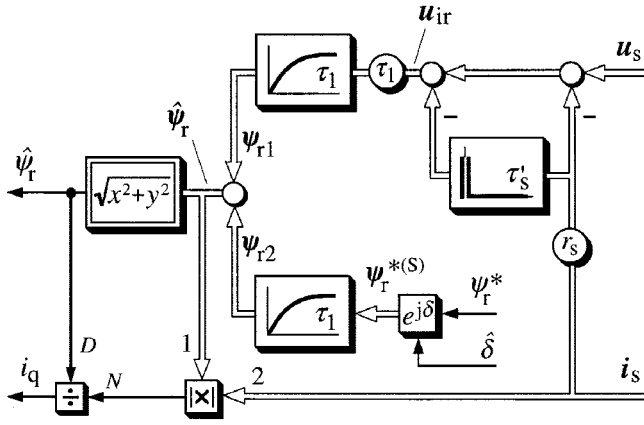


Fig. 20. Rotor flux estimator for the structure in Fig. 19.  $N$ : numerator,  $D$ : denominator.

This expression is the equivalent of the pure integral of  $\tilde{u}_{ir}$ , on condition that  $\tilde{\psi}_r = \tilde{\psi}_r^*$ . A transformation to the time domain yields two differential equations

$$\tau_1 \frac{d\psi_{r1}}{d\tau} + \psi_{r1} = \tau_1 \left( \mathbf{u}_s - r_s \mathbf{i}_s - r_s \tau'_s \frac{d\mathbf{i}_s}{d\tau} \right) \quad (39)$$

where  $\mathbf{u}_{ir}$  is expressed by the measured values of the terminal voltages and currents referring to (4), (6), and (7) and

$$\tau_1 \frac{d\psi_{r2}}{d\tau} + \psi_{r2} = \psi_r^{*(S)}. \quad (40)$$

It is specifically marked here by a superscript that  $\psi_r^{*(S)}$  is referred to in stator coordinates and, hence, is an ac variable, the same as the other variables.

The signal flow graph in Fig. 20 shows that the rotor flux vector is synthesized by the two components  $\psi_{r1}$  and  $\psi_{r2}$ , according to (39) and (40). The high gain factor  $\tau_1$  in the upper channel lets  $\psi_{r1}$  dominate the estimated rotor flux vector  $\hat{\psi}_r$  at higher frequencies. As the stator frequency reduces, the amplitude of  $\mathbf{u}_s$  reduces and  $\hat{\psi}_r$  gets increasingly determined by the signal  $\psi_{r2}$  from the lower channel. Since  $\psi_r^*$  is the input variable of this channel, the estimated value of  $\hat{\psi}_r$  is then replaced by its reference value  $\psi_r^*$  in a smooth transition. Finally, we have  $\hat{\psi}_r \approx \psi_r^*$  at low frequencies which deactivates the rotor flux controller in effect. However, the field angle  $\delta$  as the argument of the rotor flux vector is still under control through the speed controller and the  $i_q$  controller, **although the accuracy of  $\delta$  reduces**. Field orientation is finally lost at very low stator frequency. Only the frequency of the stator currents is controlled. The currents are then forced into the machine without reference to the rotor field. This provides robustness and certain stability, although not dynamic performance. In fact, the  $q$ -axis current  $i_q$  is directly derived in Fig. 20 as the current component in quadrature with what is considered to be the estimated rotor flux vector

$$i_q = \frac{\hat{\psi}_r \times \mathbf{i}_s}{|\hat{\psi}_r|} \quad (41)$$

independently of whether this vector is correctly estimated. Equation (41) is visualized in the lower left portion of the signal flow diagram in Fig. 20.

As the speed increases again, rotor flux estimation becomes more accurate, and closed-loop rotor flux control is

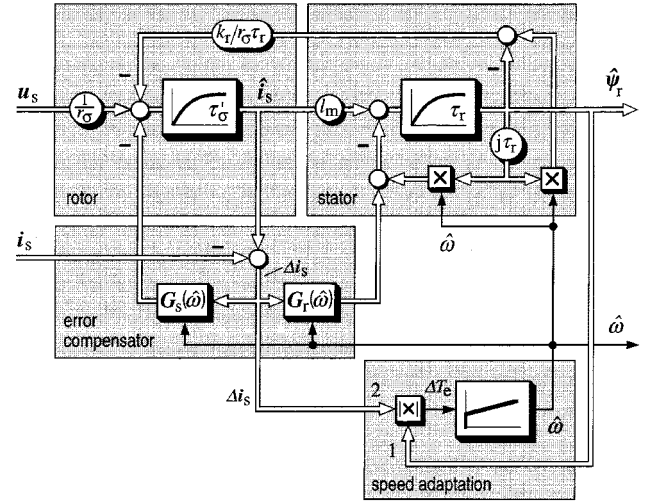


Fig. 21. Full-order nonlinear observer; the dynamic model of the electromagnetic subsystem is shown in the upper portion.

resumed. The correct value of the field angle is readjusted as the  $q$ -axis current, through (41), now relates to the correct rotor flux vector. The  $i_q$  controller then adjusts the estimated speed and, in consequence, the field angle for a realignment of the reference frame with the rotor field.

At 18 rpm, speed accuracy is reported to be within  $\pm 3$  rpm. Torque accuracy at 18 rpm is about  $\pm 0.03$  p.u. at 0.1 p.u. reference torque, improving significantly as the torque increases. Minimum parameter sensitivity exists at  $\tau_1 = \tau_r$  [12].

#### F. Adaptive Observers

The accuracy of the open-loop estimation models described in the previous chapters reduces as the mechanical speed reduces. The limit of acceptable performance depends on how precisely the model parameters can be matched to the corresponding parameters in the actual machine. It is particularly at lower speed that parameter errors have significant influence on the steady-state and dynamic performance of the drive system.

The robustness against parameter mismatch and signal noise can be improved by employing closed-loop observers to estimate the state variables and the system parameters.

1) *Full-Order Nonlinear Observer*: A full-order observer can be constructed from the machine equations (4)–(7). The stationary coordinate system is chosen,  $\omega_k = 0$ , which yields

$$\tau'_\sigma \frac{d\mathbf{i}_s}{d\tau} + \mathbf{i}_s = \frac{k_r}{r_\sigma \tau_r} (1 - j\omega \tau_r) \psi_r + \frac{1}{r_\sigma} \mathbf{u}_s \quad (42a)$$

$$\tau_r \frac{d\psi_r}{d\tau} + \psi_r = j\omega \tau_r \psi_r + l_m \mathbf{i}_s. \quad (42b)$$

These equations represent the machine model. They are visualized in the upper portion of Fig. 21. The model outputs the estimated values  $\hat{\mathbf{i}}_s$  and  $\hat{\psi}_r$  of the stator current vector and the rotor flux linkage vector, respectively.

Adding an error compensator to the model establishes the observer. The error vector computed from the model current and the machine current is  $\mathbf{e}_i = \hat{\mathbf{i}}_s - \mathbf{i}_s$ . It is used to generate correcting inputs to the electromagnetic subsystems that rep-

represent the stator and the rotor in the machine model. The equations of the full-order observer are then established in accordance with (42). We have

$$\tau'_\sigma \frac{d\hat{\mathbf{i}}_s}{d\tau} + \hat{\mathbf{i}}_s = \frac{k_r}{r_\sigma \tau_r} (1 - j\omega \tau_r) \hat{\psi}_r + \frac{1}{r_\sigma} \mathbf{u}_s - \mathbf{G}(\hat{\omega}) \Delta \mathbf{i}_s \quad (43a)$$

$$\tau_r \frac{d\hat{\psi}_r}{d\tau} + \hat{\psi}_r = j\omega \tau_r \hat{\psi}_r + l_h \hat{\mathbf{i}}_s - \mathbf{G}(\hat{\omega}) \Delta \mathbf{i}_s. \quad (43b)$$

Kubota *et al.* [13] select the complex gain factors  $\mathbf{G}_s(\hat{\omega})$  and  $\mathbf{G}_r(\hat{\omega})$  such that the two complex eigenvalues of the observer  $\lambda_{1,2 obs} = k \cdot \lambda_{1,2 mach}$ , where  $\lambda_{1,2 mach}$  are the machine eigenvalues and  $k > 1$  is a real constant. The value of  $k > 1$  scales the observer by pole placement to be dynamically faster than the machine. Given the nonlinearity of the system, the resulting complex gains  $\mathbf{G}_s(\hat{\omega})$  and  $\mathbf{G}_r(\hat{\omega})$  in Fig. 21 depend on the estimated angular mechanical speed  $\hat{\omega}$ , [13].

The rotor field angle is derived with reference to (23) from the components of the estimated rotor flux linkage vector  $\hat{\psi}_r$ .

The signal  $\hat{\omega}$  is required to adapt the rotor structure of the observer to the mechanical speed of the machine. It is obtained through a PI controller from the current error  $\Delta \mathbf{i}_s$ . In fact, the term  $\hat{\psi}_r \times \Delta \mathbf{i}_s|_z$  represents the torque error  $\Delta T_e$ , which can be verified from (9). If a model torque error exists, the modeled speed signal  $\hat{\omega}$  is corrected by the PI controller in Fig. 21, thus adjusting the input to the rotor model. The phase angle of  $\hat{\psi}_r$ , that defines the estimated rotor field angle as per (23), then approximates the true field angle that prevails in the machine. The correct speed estimate is reached when the phase angle of the current error  $\Delta \mathbf{i}_s$  and hence the torque error  $\Delta T_e$  reduce to zero.

The control scheme is reported to operate at a minimum speed of 0.034 p.u. or 50 rpm [13].

2) *Sliding Mode Observer:* The effective gain of the error compensator can be increased by using a sliding mode controller to tune the observer for speed adaptation and for rotor flux estimation. This method is proposed by Sangwongwanich and Doki [14]. Fig. 22 shows the dynamic structure of the error compensator. It is interfaced with the machine model in the same way as the error compensator in Fig. 21.

In the sliding mode compensator, the current error vector  $\Delta \mathbf{i}_s$  is used to define the sliding hyperplane. The magnitude of the estimation error  $\Delta \mathbf{i}_s$  is then forced to zero by a high-frequency nonlinear switching controller. The switched waveform can be directly used to exert a compensating influence on the machine model, while its average value controls an algorithm for speed identification. The robustness of the sliding mode approach ensures zero error of the estimated stator current. The  $H_\infty$ -approach used in [14] for pole placement in the observer design minimizes the rotor flux error in the presence of parameter deviations. The practical implementation requires a fast signal processor. The authors have operated the system at 0.036 p.u. minimum speed.

3) *Extended Kalman Filter:* Kalman filtering techniques are based on the complete machine model, which is the structure shown in the upper portion in Fig. 21, including

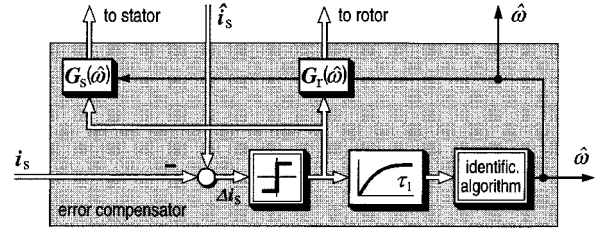


Fig. 22. Sliding mode compensator. The compensator is interfaced with the machine model in Fig. 21 to form a sliding mode observer.

the added mechanical subsystem as in Fig. 5. The machine is then modeled as a third-order system, introducing the mechanical speed as an additional state variable. Since the model is nonlinear, the extended Kalman algorithm must be applied. It linearizes the nonlinear model in the actual operating point. The corrective inputs to the dynamic subsystems of the stator, the rotor, and the mechanical subsystem are derived such that a quadratic error function is minimized. The error function is evaluated on the basis of predicted state variables, taking into account the noise in the measured signals and in the model parameter deviations.

The statistical approach reduces the error sensitivity, permitting also the use of models of lower order than the machine [15]. Henneberger *et al.* [16] have reported the experimental verification of this method using machine models of fourth and third order. This relaxes the extensive computation requirements to some extent; the implementation, though, requires floating-point signal processor hardware. Kalman filtering techniques are generally avoided due to the high computational load.

4) *Reduced-Order Nonlinear Observer:* Tajima and Hori *et al.* [17] use a nonlinear observer of reduced dynamic order for the identification of the rotor flux vector.

The model, shown in the right-hand side frame in Fig. 23, is a complex first-order system based on the rotor equation (21). It estimates the rotor flux linkage vector  $\hat{\psi}_r$ , the argument  $\hat{\delta} = \arg(\hat{\psi}_r)$  of which is then used to establish field orientation in the superimposed current control system, in a structure similar to that in Fig. 27. The model receives the measured stator current vector as an input signal. The error compensator, shown in the left frame, generates an additional model input

$$\Delta \mathbf{i}_s = \mathbf{G}_r(\hat{\omega}) \begin{bmatrix} \tau_r \frac{d\hat{\mathbf{i}}_s}{d\tau} + \left( \frac{\tau_r}{\tau'_s} + \frac{1-\sigma}{\sigma} \right) \hat{\mathbf{i}}_s \\ -\frac{\tau_r}{\sigma l_s} \left( \mathbf{u}_s + \frac{k_r}{\tau_r} (1 - j\hat{\omega} \tau_r) \hat{\psi}_r \right) \end{bmatrix} \quad (44)$$

which can be interpreted as a stator current component that reduces the influence of model parameter errors. The field transformation angle  $\hat{\delta}$  as obtained from the reduced-order observer is independent of rotor resistance variations [17].

The complex gain  $\mathbf{G}_r(\hat{\omega})$  ensures fast dynamic response of the observer by pole placement. The reduced-order observer employs a model reference adaptive system as in Fig. 14 as a subsystem for the estimation of the rotor speed. The estimated speed is used as a model input.

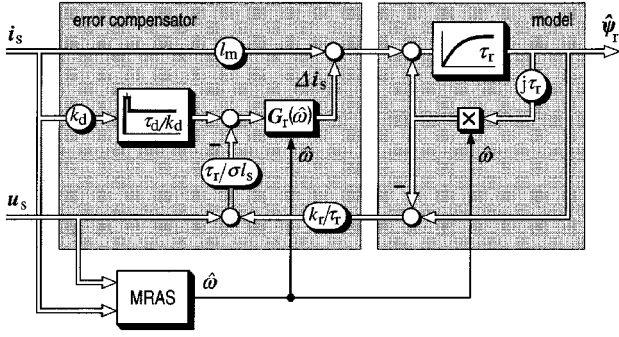


**Fig. 23.** Reduced-order nonlinear observer. The MRAS block contains the structure shown in Fig. 14;  $k_d = \tau_r/\tau'_s + (1 - \sigma)/\sigma$ .

## VI. STATOR FIELD ORIENTATION

### A. Impressed Stator Currents

Control with stator field orientation is preferred in combination with the stator model. This model directly estimates the stator flux vector. Using the stator flux vector to define the coordinate system is therefore a straightforward approach.

A fast current control system makes the stator current vector a forcing function, and the electromagnetic subsystem of the machine behaves like a complex first-order system, characterized by the dynamics of the rotor winding.

To model the system, the stator flux vector is chosen as the state variable. The machine equation in synchronous coordinates,  $\omega_k = \omega_s$ , is obtained from (10b), (6), and (7) as

$$\tau_r \frac{d\psi_s}{d\tau} + \psi_s = -j\omega_r(\tau_r\psi_s - \tau'_r l_s i_s) + l_s \left( \tau'_r \frac{di_s}{d\tau} + i_s \right) \quad (45)$$

where  $\tau'_r = \sigma\tau_r$  is the transient rotor time constant. Equation (45) defines the signal flow graph shown in Fig. 24. This first-order structure is less straightforward than its equivalent at rotor field orientation (Fig. 12), although well interpretable: since none of the state variables in (45) has an association with the rotor winding, such a state variable is reconstructed from the stator variables. The leakage flux  $\psi_\sigma = \sigma l_s i_s$  is computed from the stator current vector  $i_s$  and added to the stator flux linkage vector  $\psi_s$ . Thus, the signal  $k_r\psi_r$  is obtained, which, although reduced in magnitude by  $k_r$ , represents the rotor flux linkage vector. Such synthesized signal is then used to model the rotor winding, as shown in the upper right portion of Fig. 24. The proof that this model represents the rotor winding is in the motion-dependent term  $-j\omega_r\tau_r k_r\psi_r$ . Here, the velocity factor  $\omega_r$  indicates that the winding rotates counterclockwise at the electrical rotor frequency which, in a synchronous reference frame, applies only for the rotor winding. The substitution  $\psi_s \rightarrow \psi_r$  also explains why the rotor time constant characterizes this subsystem, although its state variable is the stator flux linkage vector  $\psi_s$ .

The stator voltage is not available as an input to generate the stator flux linkage vector. Therefore, in addition to  $i_s$ , also the derivative  $\tau'_r di_s/d\tau$  of the stator current vector must

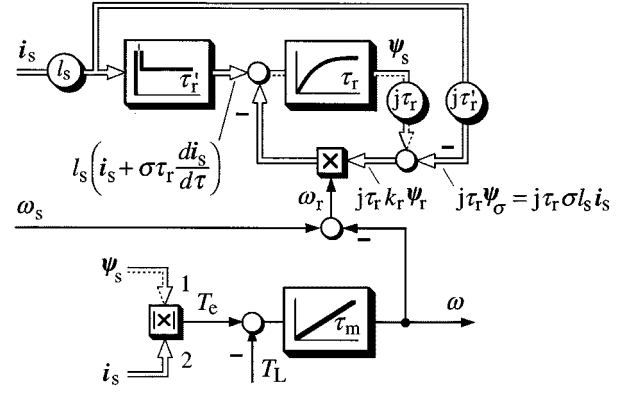


**Fig. 24.** Induction motor signal flow graph, forced stator currents; state variables: stator current, stator flux. The dotted lines represent zero signals at stator field orientation;  $\sigma\tau_r = \tau'_r$ .

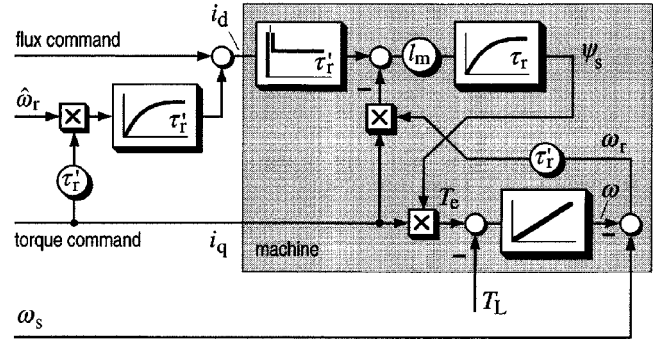


**Fig. 25.** Machine control at stator flux orientation using a dynamic feedforward decoupler.

be an input. In fact,  $\tau'_r l_s di_s/d\tau = \sigma\tau_r l_s di_s/d\tau$  is the derivative of the leakage flux vector (here multiplied by  $\tau_r$ ) which adds to the input of the  $\tau_r$  delay to compensate for the leakage flux vector  $\psi_\sigma$  that is added from its output.

To establish stator flux orientation, the stator flux linkage vector  $\psi_s$  must align with the real axis of the synchronous reference frame, and hence  $\psi_{sq} = 0$ . Therefore, the  $q$ -axis component  $d\psi_{sq}/d\tau$  at the input of the  $\tau_r$  delay must be zero, which is indicated by the dotted lines in Fig. 24. The *condition for stator flux orientation* can now be read from the balance of the incoming  $q$ -axis signals at the summing point

$$l_s \left( \tau'_r \frac{di_q}{d\tau} + i_q \right) = \omega_r \tau_r (\psi_{sd} - \sigma l_s i_d). \quad (46)$$

In a practical implementation, stator flux orientation is imposed by controlling  $\omega_r$  so as to satisfy (46). The resulting dynamic structure of the induction motor then simplifies, as shown in the shaded area of Fig. 25.

### B. Dynamic Decoupling

In the signal flow graph of Fig. 25, the torque command exerts an undesired influence on the stator flux. Xu *et al.* [18] propose a decoupling arrangement, shown in the left side of Fig. 25, to eliminate the cross coupling between the  $q$ -axis current and the stator flux. The decoupling signal depends on the rotor frequency  $\omega_r$ . An estimated value  $\hat{\omega}_r$  is therefore computed from the system variables, observing the condition





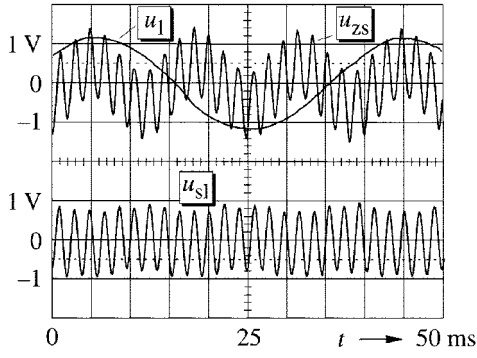


**Fig. 28.** Zero sequence component  $u_{zs}$  of the stator voltages, showing rotor slot and saturation harmonics. Fundamental frequency  $f_1 = 25$  Hz. Upper trace: before filtering, fundamental phase voltage  $u_{sl}$  shown at reduced scale for comparison. Lower trace: slot harmonics  $u_{sl}$  after filtering.

mechanical angular velocity  $\omega$  of the rotor, a bandpass filter is employed having its center frequency adaptively tuned to the rotor slot harmonic frequency  $N_r\omega + \omega_s = 2\pi/\tau_{sl}$  in (50). The time constant  $\tau_{sl}$  thus defined enters the filter transfer function

$$F_1(s) = \frac{\tau_{sl}}{(\tau_{sl}s + 1)^2} = \left(1 - \frac{1}{\tau_{sl}s + 1}\right) \frac{1}{\tau_{sl}s + 1} \quad (52)$$

which is simple to implement in software.

The signal flow graph of Fig. 29 shows how the speed estimation scheme operates. The adaptive bandpass filter in the upper portion extracts the rotor slot harmonics signal  $u_{sl}$ . The signal is shown in the lower trace of the oscillogram in Fig. 28. The filtered signal is digitized by detecting its zero crossing instants  $t_z$ . A software counter is incremented at each zero crossing by one count to memorize the digitized rotor position angle  $\vartheta$ . A slot frequency signal is then obtained by digital differentiation in the same way as from an incremental encoder. The accurate rotor speed  $\omega_{sl}$  determined by the slot count is subsequently computed with reference to (50). This signal is built from samples of the average speed, where the sampling rate decreases as the speed decreases. The sampling rate becomes very low at low speed, which accounts for a low dynamic bandwidth. Using such signal as a feedback signal in a loop speed control system would severely deteriorate the dynamic performance. This speed signal is therefore better used for parameter adaptation in a continuous speed estimator, as shown in Fig. 29.

For this purpose, an error signal is derived from two different rotor frequency signals. A first, accurate rotor frequency signal is obtained as  $\omega_{rsl} = \omega_s - \omega_{sl}$ . It serves as a reference for the rotor frequency estimator in the lower portion of Fig. 29. The second signal is the estimated rotor frequency  $\hat{\omega}_r$ , as defined by the condition for stator field orientation (46). The difference between the two signals is the error indicator.

Fig. 29 shows that the magnitudes of the two signals  $\omega_{sl}$  and  $\hat{\omega}_r$  are taken. This avoids that the sign of the error signal  $\Delta\hat{\omega}_r$  inverts in the generator mode. The error signal  $\Delta\hat{\omega}_r$  is then low-pass filtered to smooth the step increments in  $\omega_{sl}$ . The filter time constant is chosen to be as high as  $T_1 =$

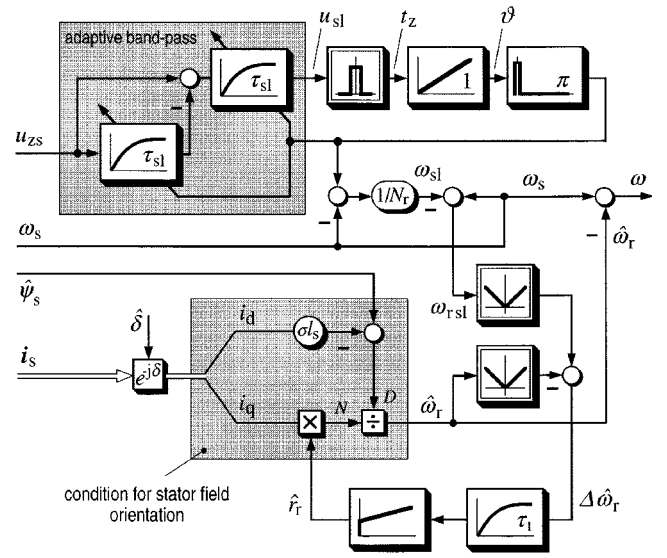


**Fig. 29.** Accurate speed identification based on rotor slot harmonics voltages.

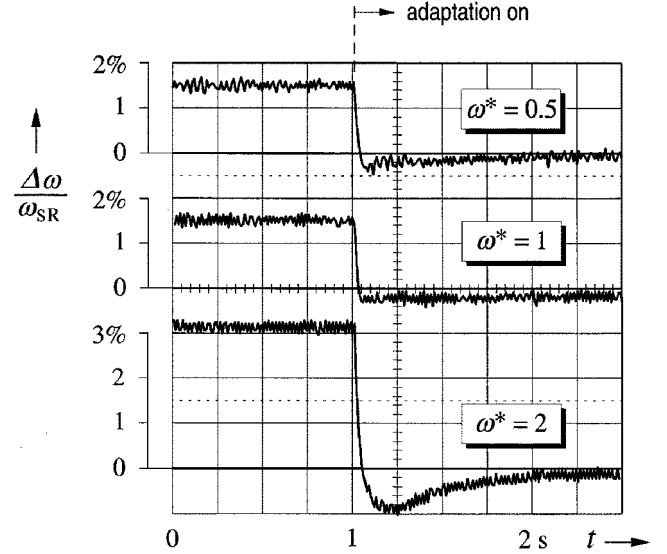


**Fig. 30.** Effect of parameter adaptation shown at different values of operating speed. Left-hand side: without parameter adaptation; right-hand side: with adaptation.

$\tau_1/\omega_{sR} = 0.7$  s to eliminate dynamic errors during acceleration at low speed. The filtered signal feeds a PI controller, the output of which eliminates the parameter errors in a simplified rotor frequency estimator

$$\hat{\omega}_r = \hat{r}_r \frac{i_q}{\psi_s - \sigma l_s i_d} \quad (53)$$

which is an approximation of (47). Although the adaptation signal of the PI controller depends primarily on the rotor resistance  $\hat{r}_r$ , it also corrects other parameter errors in (47), such as variations of the total leakage inductance  $\sigma l_s$  and the structural approximation of (47) by (53). The signal notation  $\hat{r}_r$  is nevertheless maintained.

Fig. 30 demonstrates how the rotor resistance adaptation scheme operates at different speed settings [20]. The oscillograms are recorded at nominal load torque. Considerable

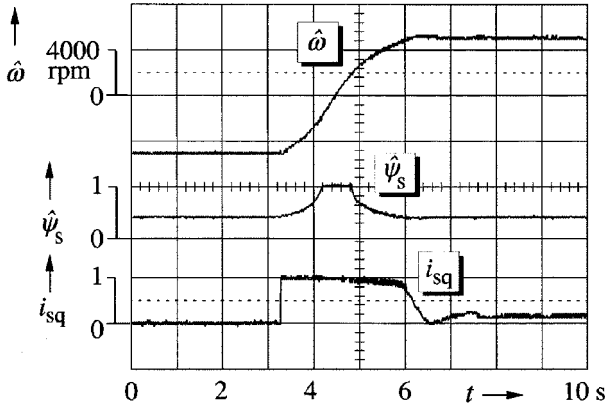


**Fig. 31.** Stator flux-oriented control without speed sensor. Speed reversal from  $-4500$  rpm to  $+4500$  rpm with field weakening.

speed errors, all referred to the rated speed  $\omega_{sR}$ , can be observed without rotor resistance adaptation. When the adaptation is activated, the speed errors reduce to less than 0.002 p.u. The overshoot of the  $\omega^* = 2$  curve is a secondary effect which is owed to the absence of a torque gain adjustment at field weakening.

## VII. PERFORMANCE OF THE FUNDAMENTAL MODEL AT VERY LOW SPEED

The important information on the field angle and the mechanical speed is conveyed by the induced voltage of the stator winding, independent of the respective method that is used for sensorless control. The induced voltage  $\mathbf{u}_i = \mathbf{u}_s - r_s \mathbf{i}_s$  is not directly accessible by measurement. It must be estimated, either directly from the difference of the two voltage space vector terms  $\mathbf{u}_s$  and  $r_s \mathbf{i}_s$ , or indirectly when an observer is employed.

In the upper speed range above a few hertz stator frequency, the resistive voltage  $r_s \mathbf{i}_s$  is small as compared with the stator voltage  $\mathbf{u}_s$  of the machine, and the estimation of  $\mathbf{u}_i$  can be made with good accuracy. Even the temperature-dependent variations of the stator resistance are negligible at higher speeds. The performance is exemplified by the oscillogram in Fig. 31, showing a speed reversal between  $\pm 4500$  rpm that includes field weakening. If operated at frequencies above the critical low-speed range, a sensorless ac drive performs as well as a vector-controlled drive with a shaft sensor; even passing through zero speed in a quick transition is not a problem.

As the stator frequency reduces at lower speed, the stator voltage reduces almost in direct proportion, while the resistive voltage  $r_s \mathbf{i}_s$  maintains its order of magnitude. It becomes the significant term at low speed. It is particularly the stator resistance  $r_s$  that determines the estimation accuracy of the stator flux vector. A correct initial value of the stator resistance is easily identified by conducting a dc test during initialization [20]. Considerable variations of the resistance take place when the machine temperature changes at varying load. These need to be tracked to maintain the system stable at low speed.

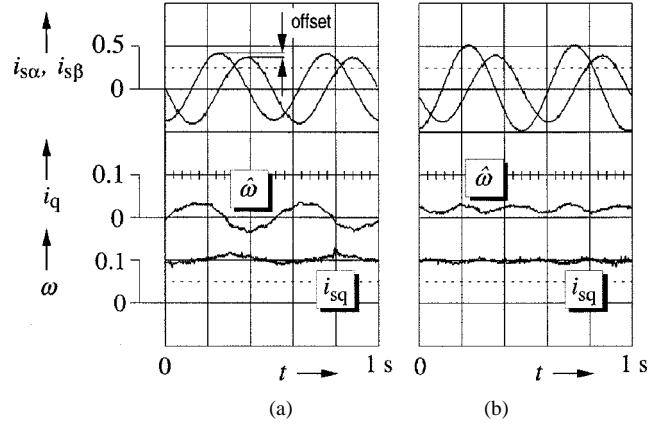


**Fig. 32.** Effect of data acquisition errors. (a) DC offset in one of the current signals. (b) Gain unbalance in the current acquisition channels.

### A. Data Acquisition Errors

As the signal level of the induced voltage reduces at low speed, data acquisition errors become significant [21]. Current transducers convert the machine currents to voltage signals which are subsequently digitized by A/D converters. Parasitic dc offset components superimposed to the analog signals appear as ac components of fundamental frequency after their transformation to synchronous coordinates. They act as disturbances on the current control system, thus generating a torque ripple [Fig. 32(a)].

Unbalanced gains of the current acquisition channels map a circular current trajectory into an elliptic shape. The magnitude of the current vector then varies at twice the fundamental frequency, producing undesired torque oscillations as shown in Fig. 32(b).

Deficiencies like current signal offset and gain unbalance have not been very detrimental so far. A lower speed limit for persistent operation is imposed anyway by drift and error problems of the flux estimation schemes. Data acquisition errors may require more attention as new solutions of the flux integration problem gradually evolve (see Section VII-D).

The basic limitation is owed to unavoidable dc offset components in the stator voltage acquisition channels. These accumulate as drift when being integrated in a flux estimator. Limiting the flux signal to its nominal magnitude leads to waveform distortions (Fig. 33). The field transformation angle as the argument of the flux vector gets modulated at four times the fundamental frequency, which introduces a ripple component in the torque producing current  $i_q$ . The resulting speed oscillations may eventually render the system unstable as the effect is more and more pronounced as the stator frequency reduces.

### B. PWM Inverter Model

At low speed, also the voltage distortions introduced by the nonlinear behavior of the PWM inverter become significant. They are caused by the forward voltage of the power devices. The respective characteristics are shown in Fig. 34. They can be modeled by an average threshold voltage  $u_{th}$  and an average differential resistance  $r_d$ , as marked by the dotted line

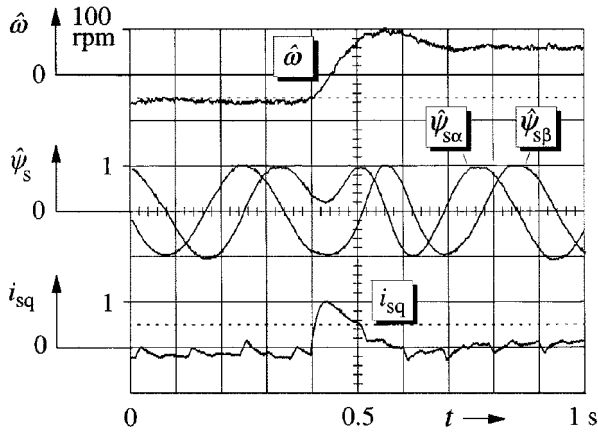


Fig. 33. Speed reversal from  $-60$  rpm to  $+60$  rpm; the estimated stator flux signal is limited to its nominal value.

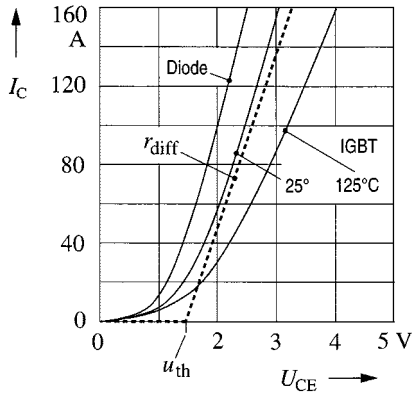


Fig. 34. Forward characteristics of the power devices.

in Fig. 34. A more accurate model is used in [22]. The differential resistance appears in series with the machine winding; its value is therefore added to the stator resistance of the machine model. Against this, the influence of the threshold voltage is nonlinear which requires a specific inverter model.

Fig. 35 illustrates the inverter topology over a switching sequence of one half cycle. The three phase currents  $i_a$ ,  $i_b$ , and  $i_c$  flow either through an active device or a recovery diode, depending on the switching state of the inverter. The directions of the phase currents, however, do not change in a larger time interval of one-sixth of a fundamental cycle. Also, the effect of the threshold voltages does not change as the switching states change in the process of pulsewidth modulation. The inverter always introduces voltage components of identical magnitude  $u_{th}$  to all three phases, while it is the directions of the respective phase currents that determine their signs. Writing the device voltages as a voltage space vector (3) defines the threshold voltage vector

$$\mathbf{u}_{th} = u_{th} \text{sign}(i_a) + a u_{th} \text{sign}(i_b) + a^2 u_{th} \text{sign}(i_c) \quad (54)$$

where  $a = \exp(j2\pi/3)$ . To separate the influence of the stator currents, (54) is expressed as

$$\mathbf{u}_{th} = 2 u_{th} \cdot \text{sec}(\mathbf{i}_s) \quad (55)$$

where

$$\text{sec}(\mathbf{i}_s) = \frac{1}{2} (\text{sign}(i_a) + a \text{sign}(i_b) + a^2 \text{sign}(i_c)) \quad (56)$$

is the sector indicator [21], a complex nonlinear function of  $\mathbf{i}_s(t)$  of unity magnitude. The sector indicator marks the respective  $\pm 30^\circ$ -sector in which  $\mathbf{i}_s$  is located. Fig. 36 shows the six discrete locations that the sector indicator  $\text{sec}(\mathbf{i}_s)$  can assume in the complex plane.

The reference signal  $\mathbf{u}^*$  of the PWM controls the stator voltages of the machine. It follows a circular trajectory in the steady state. Owing to the threshold voltages of the power devices, the average value  $\mathbf{u}_{av}$  of the stator voltage vector  $\mathbf{u}_s$ , taken over a switching cycle, describes trajectories that are distorted and discontinuous. Fig. 37 shows that the fundamental amplitude of  $\mathbf{u}_{av}$  is less than its reference value  $\mathbf{u}^*$  at motoring and larger at regeneration. In addition, the voltage trajectories exhibit strong sixth-harmonic components. Since the threshold voltage does not vary with stator frequency as the stator voltage does, the distortions are more pronounced when the stator frequency, and hence the stator voltages, are low. The latter may even exceed the commanded voltage in magnitude, which then makes correct flux estimation and stable operation of the drive impossible. Fig. 38 demonstrates how the voltage distortion caused by the inverter introduces oscillations in the current and the speed signals.

Using the definitions (55) and (56), an estimated value  $\hat{\mathbf{u}}_s$  of the stator voltage vector is obtained from the PWM reference voltage vector  $\mathbf{u}^*$  as

$$\hat{\mathbf{u}}_s = \mathbf{u}^* - \mathbf{u}_{th} - r_d \mathbf{i}_s \quad (57)$$

where the two subtracted vectors on the right represent the inverter voltage vector. The inverter voltage vector reflects the respective influence of the threshold voltages through  $\mathbf{u}_{th}$  and of the resistive voltage drop of the power devices through  $r_d \mathbf{i}_s$ . A signal flow graph of the inverter model (57) is shown in the left-hand side of Fig. 39.

Note that  $u_{th}$  is the threshold voltage of the power devices, while  $\mathbf{u}_{th}$  is the resulting threshold voltage vector. Therefore, from (55), we have the unusual relationship  $|\mathbf{u}_{th}| = 2u_{th}$ . The reason is that, unlike in a balanced three-phase system, the three phase components in (54) have the same magnitude, which is unity.

### C. Identification of the Inverter Model Parameters

The threshold voltage  $u_{th}$  can be identified during self-commissioning from the distortions of the reference voltage vector  $\mathbf{u}^*$  [21], [22]. In this process, the components  $u_{\alpha}^*$  and  $u_{\beta}^*$  of the reference voltage vector are acquired while the current controllers inject sinusoidal currents of very low frequency into the stator windings. In such condition, the machine impedance is dominated by the stator resistance. The stator voltages are then proportional to the stator currents.

Deviations from a sinewave of the reference voltages that control the pulsewidth modulator are therefore caused by the inverter. They are detected by subtracting the fundamental components from the reference voltages, which then yields square wave like, stepped waveforms as shown in Fig. 40. The fundamental components are extracted from sets of synchronous samples of  $u_{\alpha}^*$  and  $u_{\beta}^*$  by a fast Fourier transform.

The differential resistance of the power devices,  $r_d$  in (57), establishes a linear relation between the load current and its



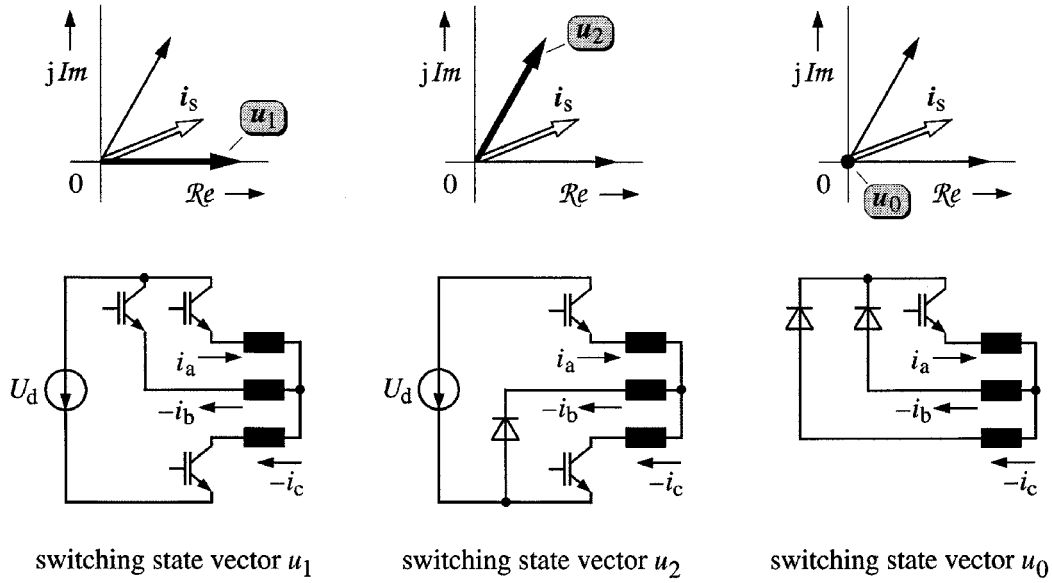


Fig. 35. Effect of pulsewidth modulation of the forward voltages of the power semiconductors.

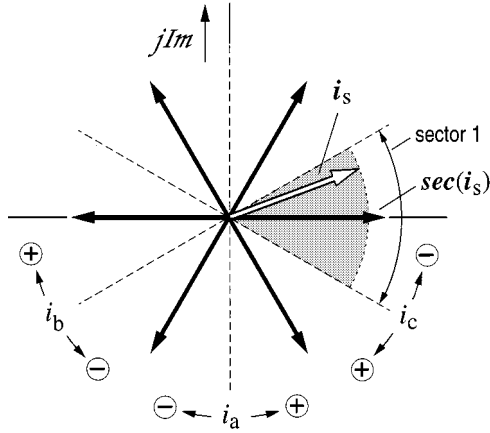


Fig. 36. The six possible locations of the sector indicator  $\text{sec}(i_s)$ ; the dotted lines indicate the transitions at which the signs of the respective phase currents change.

influence on the inverter voltage. Functionally, it adds to the resistance  $r_s$  of the stator windings and hence influences also upon the transient stator time constant of the induction motor, and on the design parameters of the current controllers. The value  $(r_s + r_d)$  can be estimated by an on-line tuning process described in Section VII-E.

#### D. Stator Flux Estimation

The inverter model (57) is used to compensate the non-linear distortions introduced by the power devices. The model estimates the stator voltage vector  $\mathbf{u}_s$  that prevails at the machine terminals, using the reference voltage vector  $\mathbf{u}^*$  of the PWM as the input variable. The inverter model thus enables a more accurate estimation of the stator flux linkage vector. This signal flow graph is shown in the left-hand side of Fig. 39.

The right-hand side of Fig. 39 shows that the stator flux vector is obtained by pure integration [21], thus avoiding the estimation error and bandwidth limitation associated with

using a low-pass filter. The method necessarily incorporates the identification of a time-varying vector  $\hat{\mathbf{u}}_{\text{off}}$  that represents the offset voltages.

The defining equation of the stator flux estimator is

$$\hat{\psi}_s = \int (\hat{\mathbf{u}}_s - \hat{r}_s \mathbf{i}_s + \hat{\mathbf{u}}_{\text{off}}) d\tau \quad (58)$$

where  $\hat{\mathbf{u}}_s$  is the estimated stator voltage vector (57) and

$$\hat{\mathbf{u}}_{\text{off}} = k_1 (\psi_s^* - \hat{\psi}_s) e^{j\hat{\delta}} \quad (59)$$

is the estimated offset voltage vector, while  $\hat{\delta}$  is the estimated stator field angle. The offset voltage vector  $\hat{\mathbf{u}}_{\text{off}}$  in (58) is determined such that the estimated stator flux vector  $\hat{\psi}_s$  rotates close to a circular trajectory of radius  $\psi_s^*$ , which follows from (58) and (59). The integrator drift is thus eliminated, while the essential information on the field angle  $\hat{\delta} = \arg(\hat{\psi}_s)$  is maintained.

The stator field angle  $\hat{\delta}$  is computed as

$$\hat{\delta} = \arctan(\psi_{s\beta}/\psi_{s\alpha}) \quad (60)$$

which is symbolized by the  $\tan^{-1}$  function block in Fig. 39. The magnitude of the stator flux linkage vector is then obtained by

$$\hat{\psi}_s = \hat{\psi} e^{-j\hat{\delta}}. \quad (61)$$

This value is used in (59) to determine the vector of the actual offset voltage. The stator frequency signal is computed by

$$\omega_s = \frac{d\hat{\delta}}{d\tau} \quad (62)$$

from which the angular mechanical velocity  $\omega$  is determined with reference to (20) and (44).

#### E. Stator Resistance Estimation

An important measure to improve the low-speed performance is the accurate online adaptation of the stator resistance, which is the most relevant parameter in sensorless control. Kubota *et al.* [23] use the observer structure shown in

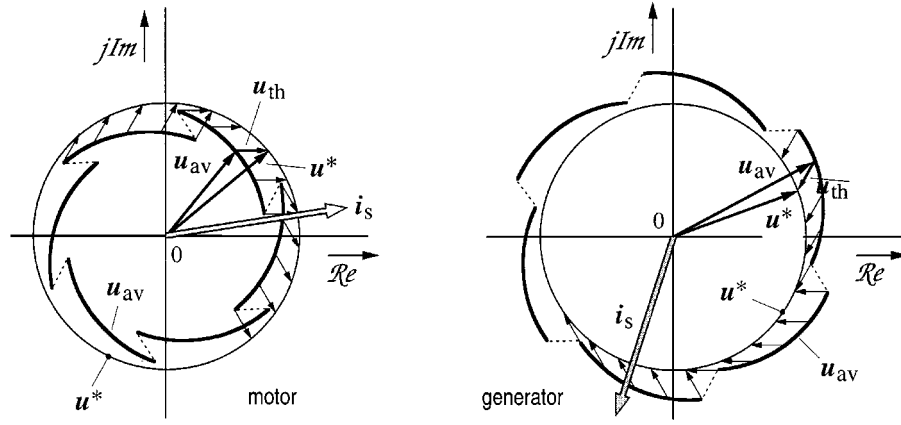


**Fig. 37.** The effect of inverter nonlinearity. The trajectories  $\mathbf{u}_{av}$  represent the average stator voltage (switching harmonics excluded).

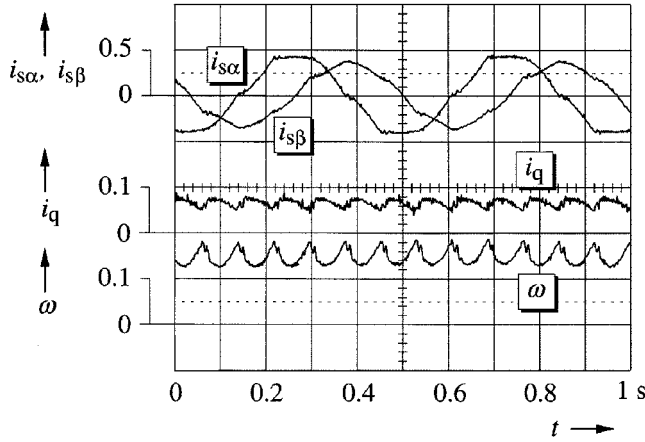


**Fig. 38.** Current waveform distortions and speed oscillations caused by the threshold voltage of the inverter devices; sensorless control at 2 Hz stator frequency, bipolar power transistors used in the inverter.

Fig. 21 to determine the component of the error vector  $\mathbf{e}_i$  in the direction of the stator current vector, which is proportional to the deviation of the model parameter  $\hat{r}_s$  from the actual stator resistance. The identifying equation is therefore

$$\hat{r}_s = -\frac{1}{\tau_1} \int (\mathbf{e}_i \circ \hat{\mathbf{i}}_s) d\tau. \quad (63)$$

The identification delay of this method is reported as 1.4 s.

A faster algorithm relies on the orthogonal relationship in steady state between the stator flux vector and the induced voltage [21]. The inner product of these two vectors is zero, shown as follows:

$$\hat{\psi}_s(q) \circ \hat{\mathbf{u}}_i = \hat{\psi}_s(q) \circ (\hat{\mathbf{u}}_s - \hat{r}_s \hat{\mathbf{i}}_s) = 0. \quad (64)$$

The stator flux vector in this equation must not depend on the stator resistance  $r_s$  to facilitate the estimation of  $r_s$ . An expression  $\hat{\psi}_s(q)$  is therefore derived from the instantaneous reactive power  $q = \mathbf{u}_s \times \mathbf{i}_s|_z$ , which notation describes the  $z$  component of the vector product of the stator voltage and current vector.

The rotor equation in terms of  $\hat{\mathbf{i}}_s$  and  $\hat{\psi}_s$  is obtained in synchronous coordinates,  $\omega_k = \omega_s$ , from (4)–(7) as

$$\tau'_{sr} \frac{d\hat{\mathbf{i}}_s}{d\tau} + \hat{\mathbf{i}}_s = -j\omega_r \tau'_{sr} \hat{\mathbf{i}}_s + \frac{1}{r_{sr}} \left( \frac{1}{\tau_r} - j\omega \right) \hat{\psi}_s + \frac{1}{r_{sr}} \mathbf{u}_s \quad (65)$$

where  $\tau'_{sr} = \sigma l_s / r_{sr}$  and  $r_{sr} = (r_s + l_s / l_r \cdot r_r)$ . Equation (65) is now externally multiplied by the vector  $\hat{\mathbf{i}}_s$ , from which

$$\mathbf{u}_s \times \hat{\mathbf{i}}_s - \sigma l_s \frac{d\hat{\mathbf{i}}_s}{d\tau} \times \hat{\mathbf{i}}_s - j\omega_r \sigma l_s \hat{\mathbf{i}}_s \times \hat{\mathbf{i}}_s = \left( j\omega - \frac{1}{\tau_r} \right) \hat{\psi}_s \times \hat{\mathbf{i}}_s \quad (66)$$

is obtained. This operation eliminates the stator and the rotor resistances from (65) where these parameters are contained in  $\tau'_{sr}$ . Taking the  $z$  component of all terms in (66) and assuming field orientation,  $\psi_{sd} = \psi_s$  and  $\psi_{sq} = 0$ , we have

$$\hat{\psi}_s(q) = \frac{(u_q i_d - u_d i_q) - \omega_r \sigma l_s i_s^2 + \sigma l_s \left( i_q \frac{di_d}{d\tau} - i_d \frac{di_q}{d\tau} \right)}{\omega i_d + \frac{i_q}{\tau_r}}. \quad (67)$$

The stator flux value thus defined does not depend on the stator resistance.

To reduce the online computation time for the estimation of  $r_s$ , (64) is transformed to a reference frame that aligns with the current vector. The current reference frame ( $xy$ -frame) rotates in synchronism and is displaced with respect to stationary coordinates by the phase angle  $\gamma(\tau)$  of the stator current, as shown in Fig. 41. We have  $\hat{\mathbf{i}}_s^{(C)} = \hat{\mathbf{i}}_s^{(S)} \cdot \exp(-j\gamma)$  and consequently  $i_{sx} = i_s$  and  $i_{sy} = 0$ . Of the superscripts, (S) refers to stator coordinates and (C) refers to current coordinates.

The estimated value of the stator resistance is obtained as the solution of (64) in current coordinates

$$\hat{r}_s = \frac{\hat{u}_{sx} - \frac{\hat{\psi}_{sy}}{\hat{\psi}_{sx}} \hat{u}_{sy}}{\hat{i}_{sx}} = \frac{\hat{u}_{sx} - \omega_s \hat{\psi}_s(q) \sin(\gamma - \hat{\delta})}{\hat{i}_s} \quad (68)$$

using the geometrical relationships

$$\frac{\hat{\psi}_{sy}}{\hat{\psi}_{sx}} = \tan(\gamma - \hat{\delta}) \quad (69)$$

and

$$u_{sy} = \hat{u}_i \cos(\gamma - \hat{\delta}) \quad (70)$$

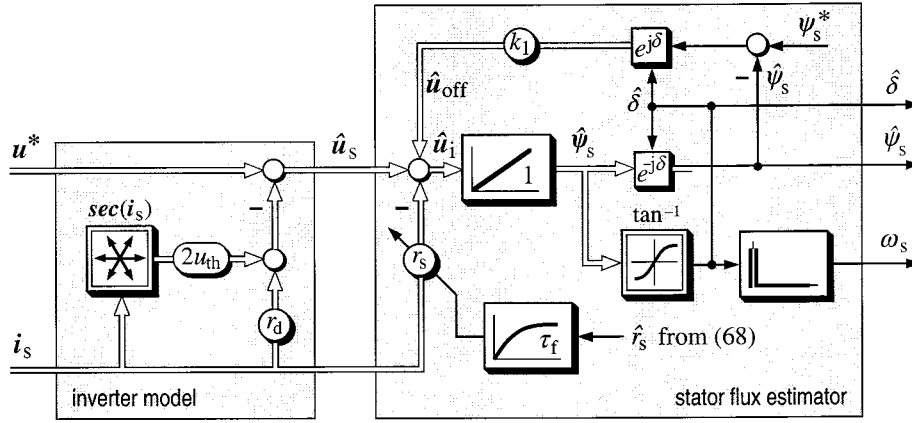


Fig. 39. Signal flow graph of the inverter model and the offset compensated stator flux estimator.

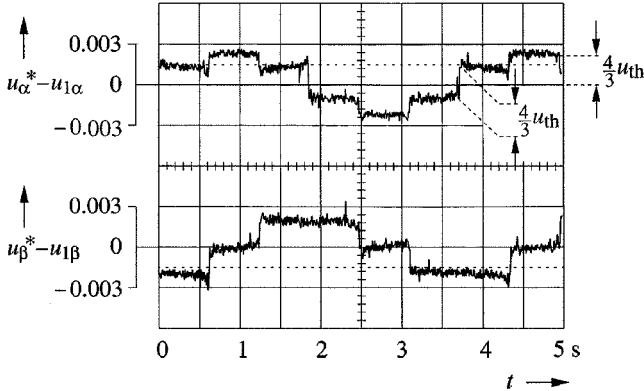


Fig. 40. The distortion voltage generated by the inverter; components in stationary coordinates.

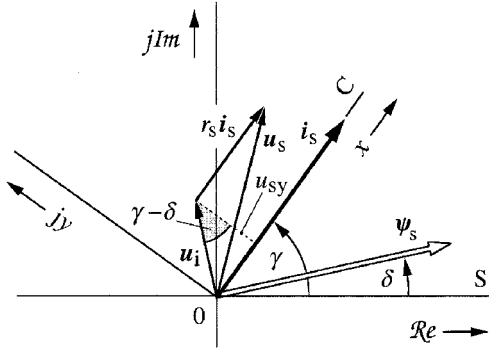


Fig. 41. Vector diagram illustrating the estimation of the stator resistance;  $S$  marks the stationary reference frame ( $\alpha, \beta$ ) and  $C$  marks the current reference frame ( $x, y$ ).

which can be taken from the vector diagram shown in Fig. 41. Furthermore, we have in a steady state

$$\hat{u}_i = \omega_s \hat{\psi}_s(q). \quad (71)$$

The estimated stator resistance value  $\hat{r}_s$  from (68) is then used as an input signal to the stator flux estimator Fig. 39. It adjusts its parameter through a low-pass filter. The filter time constant  $T_f = \omega_s R \tau_f$  is about 100 ms.

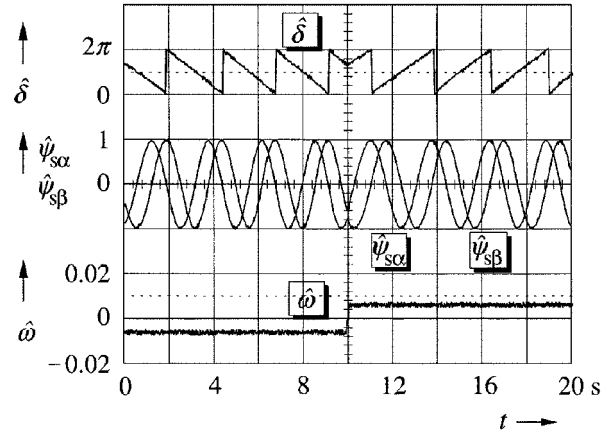


Fig. 42. Speed reversal at 10 rpm, and fundamental frequency  $f_1 = \omega_s / 2\pi = \pm 0.33$  Hz ( $\omega_s = \pm 0.007$ ).

#### F. Low-Speed Performance Achieved by Improved Models

The oscillogram shown in Fig. 42 demonstrates the dynamic performance at very low speed, exemplified by a speed reversal from  $-10$  rpm to  $+10$  rpm ( $f_s = \omega_s / 2\pi = \pm 0.33$  Hz,  $\omega_s = \pm 0.007$ ). The recorded components  $\psi_{s\alpha}$  and  $\psi_{s\beta}$  of the estimated stator flux linkage vector exhibit sinusoidal waveforms without offset, drift, or distortion, and smooth crawling speed is achieved. Fig. 43 shows the response to load step changes of rated magnitude while the speed is maintained constant at 5 rpm. This corresponds to operating at a stator frequency of 0.16 Hz ( $\omega_s = 0.003$ ) during the no-load intervals. Finally, the performance of the stator resistance identification scheme is demonstrated in Fig. 44. The stator resistance is increased by 25% in a step change fashion. The disturbance causes a sudden deviation from the correct field angle, which temporarily produces an error in  $i_q$ . The correct value of  $r_s$  is identified after a short delay, and  $i_q$  readjusts to its original magnitude.

#### G. Low-Speed Estimation by Field Weakening

At very low stator frequency, the induced voltage is small and its influence on the measured terminal quantities is difficult to detect (see Section II-D). Depenbrock [24] proposes

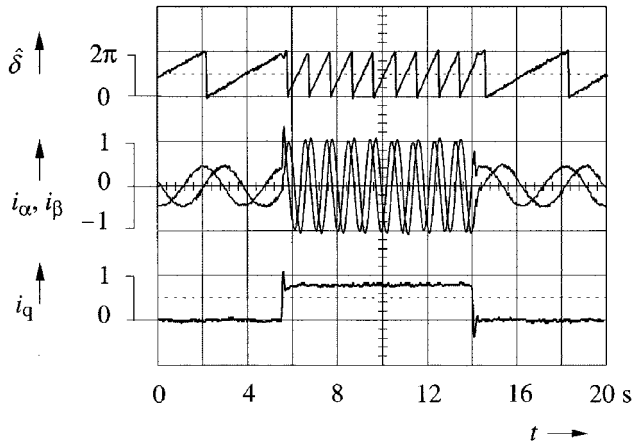


**Fig. 43.** Constant speed operation at 5 rpm ( $f_1 = \omega_s/2\pi = \pm 0.16$  Hz,  $\omega_s = \pm 0.003$ ), with load step changes of rated magnitude applied.

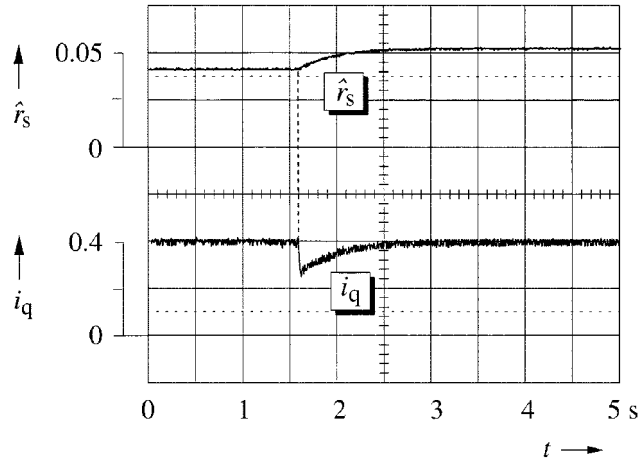


**Fig. 44.** Identification of the stator resistance, demonstrated by a 25% step increase of the resistance value.

not reducing the stator frequency below a certain minimum level  $\omega_{s \min}$ , a level that still permits identifying the mechanical speed. At values below that level, the speed is controlled through the magnetic excitation of the machine. The method makes use of the fact that the slip, or rotor frequency, increases at field weakening. This is demonstrated by inserting (47) into (20) and considering the steady state,  $d/d\tau = 0$ , from which

$$\omega = \omega_{s \min} - \omega_r = \omega_{s \min} - \frac{l_s i_q}{\tau_r (\psi_{sd} - \sigma l_s i_d)} \quad (72)$$

is obtained. The equation is used to demonstrate how controlled operation at lower speed  $\omega < \omega_{s \min}$  is achieved while operating the machine at constant stator frequency  $\omega_s = \omega_{s \min}$ . For this purpose, field weakening is introduced by reducing  $i_d$ . This makes  $\psi_{sd}$  reduce after a time delay that depends on  $\tau'_r$  and  $\tau_r$  (see Fig. 24). The rotor frequency term on the right-hand side in (72) then increases as the denominator decreases, and the numerator increases as the product  $\psi_{sd} i_q$  is constant at a given load torque (9), provided that field orientation exists.

The following oscillograms illustrate the method. Fig. 45 shows controlled operation at locked rotor while the torque is

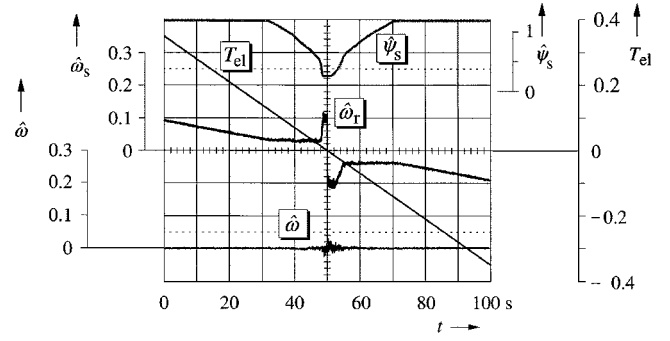


**Fig. 45.** Locked rotor test to demonstrate low-speed torque control by field weakening; stator and rotor frequency are controlled to remain outside the region  $|\omega_s|, |\omega_r| < \omega_{s \min}$  to enable stator flux identification.

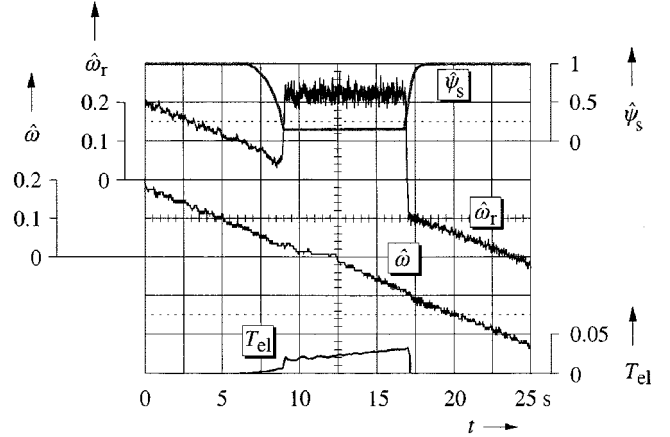


**Fig. 46.** Quasi-steady-state transition through zero speed at low load; through field weakening and by forcing an additional torque, stator and rotor frequency are kept outside the region  $|\omega_s|, |\omega_r| < \omega_{s \min}$ .

continuously varied from positive to negative values. Since  $\omega = 0$ ,  $\omega_s = \omega_r$  follows. The stator frequency reduces as  $T_{el}$  reduces until  $\omega_{s \min}$  is reached and field weakening begins. As the machine torque becomes negative, the stator frequency is abruptly changed from  $\omega_{s \min}$  to  $-\omega_{s \min}$  which makes the rotor frequency also change its sign. The torque magnitude subsequently increases until the machine excitation has reached its nominal value. Thereafter, the torque is again controlled through the stator frequency.

When operating at very low speed at light or zero load, the level of field weakening must be very small. Establishing the required slip to maintain the stator frequency high enough for speed estimation may then become difficult. Fig. 46 shows that a small torque component, although not commanded, is intentionally introduced to increase the slip. This and the time delay required for changing the machine flux is tolerable for certain applications, e.g., in railway traction drives [22].

## VIII. SENSORLESS CONTROL THROUGH SIGNAL INJECTION

Signal injection methods exploit machine properties that are not reproduced by the fundamental machine model described in Section II-B. The injected signal excites the machine at a much higher frequency than that of the funda-



mental field. The resulting high-frequency currents generate flux linkages that close through the leakage paths in the stator and the rotor, leaving the mutual flux linkage with the fundamental wave almost unaffected. The high-frequency effects can be therefore considered superimposed to and independent of the fundamental behavior of the machine. High-frequency signal injection is used to detect anisotropic properties of the machine.

#### A. Anisotropies of an Induction Machine

A magnetic anisotropy can be caused by saturation of the leakage paths through the fundamental field. The spatial orientation of the anisotropy is then correlated with the field angle  $\delta$ , which quantity can be identified by processing the response of the machine to the injected signal. Other anisotropic structures are the discrete rotor bars in a cage rotor. Different from that, a rotor may be custom designed so as to exhibit periodic variations within a fundamental pole pitch of local magnetic or electrical characteristics. Examples are variations of the widths of the rotor slot openings [25] of the depths at which the rotor bars are buried below the rotor surface, or of the resistance of the outer conductors in a double cage, or deep bar rotor [26]. Detecting such anisotropy serves to identify the rotor position angle, the changes of which are used to obtain the shaft speed.

Anisotropic conditions justify the definition of a coordinate system that aligns with a particular anisotropy. Considering the case of saturation-induced anisotropy, the maximum flux density occurs in the  $d$  axis of a field-oriented coordinate system. The fundamental field saturates the stator and rotor iron in the  $d$  region, there producing higher magnetic resistivity of the local leakage paths. The stator and rotor currents in the conductors around the saturated  $d$  region excite leakage fluxes having a dominating  $q$  component. The total leakage inductance component  $l_{\sigma q}$  then reduces, while the component  $l_{\sigma d}$  of the unsaturated  $q$  region remains unaffected. Such conditions lead to  $l_{\sigma q} < l_{\sigma d}$  in a saturated machine.

A more general definition of an anisotropy related reference frame locates the  $d$  axis at that location of the airgap circumference that exhibits the maximum high-frequency time constant. This associates the  $d$  axis with the maximum total leakage inductance or with the minimum resistivity of conductors on the rotor surface.

There is generally more than one anisotropy present in an induction motor. The existing anisotropies have different spatial orientations such as the actual angular position of the fundamental field, the position of the rotor bars within a rotor bar pitch, and, if applicable, the angular position within a fundamental pole pair of a custom designed rotor. The response to an injected high-frequency signal necessarily reflects all anisotropies, field-dependent and position-dependent. While intending to extract information on one particular anisotropy, the other anisotropies act as disturbances.

#### B. Signal Injection

The injected signals may be periodic, creating either a high-frequency revolving field or an alternating field in a specific, predetermined spatial direction. Such signals can

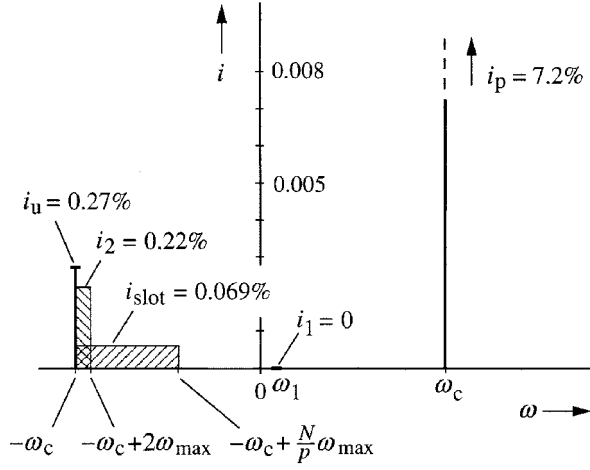


**Fig. 47.** Measured spectral current components from an unexcited machine having two anisotropies, operated in a speed range  $\omega = 0 \dots \omega_{\max} = 2\pi \cdot 10$  Hz (measurement data taken from [28]).

be referred to as carriers, being periodic at the carrier frequency with respect to space or time. The carrier signals, mostly created by additional components of the stator voltages, are modulated by the actual orientations in space of the machine anisotropies. The carrier frequency components are subsequently extracted from the machine current waveforms. They are demodulated and processed to retrieve the desired information.

Instead of injecting a periodic carrier, the high-frequency content of the switched waveforms in a PWM-controlled drive system can be exploited for the same purpose. The switching of the inverter produces a perpetual excitation of the high-frequency leakage fields. Their distribution in space is governed by the anisotropies of the machine. Measuring and processing of adequate voltage or current signals permits identifying their spatial orientations.

#### C. Injection of a Revolving Carrier

A polyphase carrier rotating at frequency  $\omega_c$  can be generated by the voltage space vector

$$\mathbf{u}_c = u_c \cdot e^{j(\omega_c)t} \quad (73)$$

which is the controlling voltage of the PWM as shown in Fig. 47. The modulation by the machine anisotropies reflects in a space vector  $\mathbf{i}_c$  of carrier frequency  $\omega_c$ , appearing as a component of the measured stator current vector  $\mathbf{i}_s$ . It is separated by a bandpass filter (BPF) from the fundamental current  $\mathbf{i}_{s1}$  of lower frequency and from the switching harmonics of higher frequencies.

A single anisotropy having one spatial cycle per pole pitch is typical for saturation effects or for a custom-engineered machine. Such anisotropy is characterized by a total leakage inductance tensor

$$\mathbf{l}_{\sigma}^{(X)} = \begin{bmatrix} l_{\sigma d} & 0 \\ 0 & l_{\sigma q} \end{bmatrix} \quad (74)$$

being defined with reference to a coordinate system ( $X$ ) that rotates at  $\omega_x$  in synchronism with the anisotropy under consideration ( $xy$  coordinates). The  $x$  axis coincides with the most saturated region.

To compute the carrier space vector  $\mathbf{i}_c$ , (73) is multiplied by  $\exp(-j\omega_x)$ , which transforms the equation to  $xy$  coordinates. The high-frequency components are described by the differential equation

$$\mathbf{u}_c^{(X)} = u_c \cdot e^{j(\omega_c - \omega_x)t} = \mathbf{l}_\sigma^{(X)} \frac{d\mathbf{i}_c}{dt} \quad (75)$$

which is solved for  $\mathbf{i}_c$ . Considering  $\omega_c \gg \omega_x$  leads to the solution

$$\mathbf{i}_c^{(X)} = \frac{-j\omega_c}{2\omega_c l_{sd} l_{sq}} \left[ (l_{sd} + l_{sq})e^{+j(\omega_c - \omega_x)t} + (l_{sd} - l_{sq})e^{-j(\omega_c - \omega_x)t} \right] \quad (76)$$

which is subsequently transformed back to the stationary reference frame

$$\begin{aligned} \mathbf{i}_c^{(S)} &= \frac{-j\omega_c}{2\omega_c l_{\sigma d} l_{\sigma q}} \left[ (l_{\sigma d} + l_{\sigma q}) e^{j(\omega_c t)} \right. \\ &\quad \left. + (l_{\sigma d} - l_{\sigma q}) e^{j((-\omega_c + 2\omega_x)t)} \right] \\ &= \mathbf{i}_p + \mathbf{i}_n. \end{aligned} \quad (77)$$

The result shows the existence of a current space vector  $\mathbf{i}_p$ , rotating at carrier frequency  $\omega_c$  in a positive direction, and a space vector  $\mathbf{i}_n$  that rotates at the angular velocity  $-\omega_c + 2\omega_x$ , i.e., in a negative direction. The latter component must be processed to extract the angular orientation  $\omega_x t$  of the particular anisotropy.

Rotating at the frequency of the carrier signal, the trajectory (77) of the current vector  $\mathbf{i}_c$  in fact follows an elliptic path. The axis ratio of the ellipse is  $l_{sq}/l_{sd}$ , a close to unity value that ranges between 0.9 and 0.96 [25], [27]. It is therefore difficult to identify the angular inclination of the ellipse and thus determine the angular orientation of the anisotropy. A direct extraction is problematic, as the characterizing component  $\mathbf{i}_n$  is very small, being superimposed by the larger positive sequence current vector  $\mathbf{i}_p$  and contaminated by the effect of other anisotropies and disturbances. Finally, all these signals are buried under the much larger fundamental current  $\mathbf{i}_{s1}$  and under the switching harmonics.

To give an example, the current amplitudes  $i_p/i_{1R}$  and  $i_n/i_{sR}$  from [27], referring to the rated fundamental current  $i_{sR}$ , are shown in Fig. 47. The values are measured from an induction machine at zero fundamental excitation,  $i_1 = 0$ , so as to avoid saturation generating an additional anisotropy. However, the rotor has an engineered anisotropy of  $l_{\sigma q}/l_{\sigma d} = 0.91$  [25]. There are three categories of negative sequence currents.

- The current  $i_2$  at frequency  $-\omega_c + 2\omega$  is caused by the engineered rotor anisotropy. Its harmonic spectrum spreads between  $-\omega_c$  and  $-\omega_c + 2\omega_{\max}$  when the machine speed  $\omega$  varies between 0 and  $\omega_{\max}$ , where  $\omega_{\max} = 2\pi \cdot 10$  Hz is an assumed maximum value in Fig. 48. This frequency component carries the speed information; its magnitude  $i_2 = 0.022 i_{2R}$  is extremely low.
- The current  $i_{\text{slot}}$  at frequency  $-\omega_c + N/p\omega$  is caused by the discrete rotor slots; it extends over the frequency

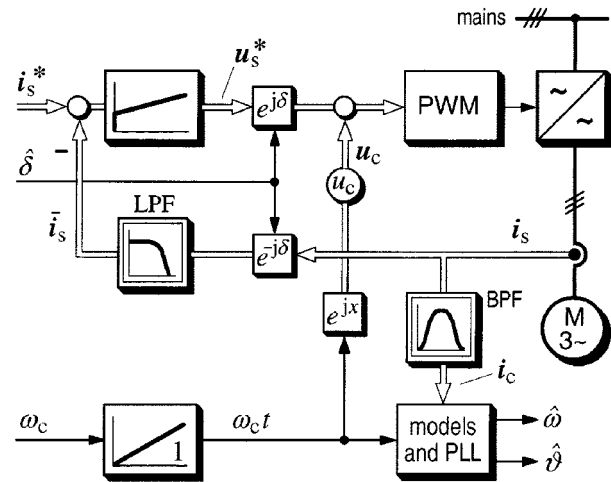


**Fig. 48.** Current control system and signal injection for the identification of anisotropies through an injected revolving carrier.

range  $-\omega_c$  to  $-\omega_c + N/p \omega_{\max}$ , where  $N$  is the number of rotor slots and  $p$  is the number of pole pairs.

- The current  $i_u$  at frequency  $-\omega_c$  originates from winding asymmetries and from gain unbalances in the stator current acquisition circuits. Note that this disturbance is in very close spectral proximity to the speed related component  $i_2$ ; both converge to the same frequency at  $\omega = 0$ . Also,  $i_u > i_2$  in this example.

If this machine was fully fluxed and loaded, another negative sequence current  $i_{\text{sat}}$  would appear at frequency  $-\omega_c + 2\omega_s$ . Also, this component has an extremely low spectral distance  $2(\omega_s - \omega)$  from the component  $i_2$ , where  $\omega_s - \omega$  is the slip frequency.

The distribution of the significant negative sequence spectra in Fig. 48 indicates that it is almost impossible to separate these signals by filtering [28].

1) *Speed and Position Estimation Based on Anisotropies*: Degner and Lorenz [25] use a dynamic model of the mechanical subsystem of the drive motor to enable spectral separation. The modeled position angle  $\hat{\theta}$  is synchronized with the revolving machine anisotropy in a closed phase-locked loop (PLL). The machine anisotropy is custom engineered in this case. Additional models of other dominant anisotropies serve to generate compensation signals which eliminate those spectral components that are difficult to separate by filtering (see Section VIII-C). Fig. 48 shows the basic structure. An estimated field angle  $\hat{\delta}$  is used to perform current control in field coordinates. A revolving carrier of 250 Hz is injected through the voltage space vector  $\mathbf{u}_c$  as defined by (73). The carrier frequency components in the measured machine currents are attenuated by a low-pass filter (LPF) in the feedback path of the current controller. A BPF extracts the carrier generated current vector  $\mathbf{i}_c$ .

A signal flow graph of the speed and rotor position estimator is shown in Fig. 49. The carrier generated space vector  $\mathbf{i}_c$  is transformed to a  $+\omega_c$ -reference frame in which  $\mathbf{i}_p$  appears as a complex constant. Its contribution is nullified through the feedback action of an integrator. The remaining signal  $\mathbf{i}_n$  contains all negative sequence components. It



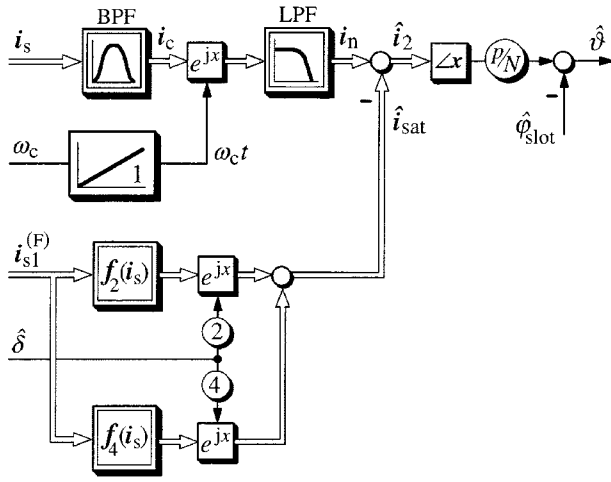


**Fig. 50.** Modeling and compensation of the saturation-induced anisotropy for a position estimation scheme based on rotor slots.

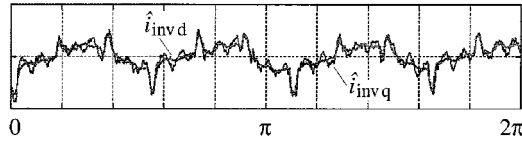


**Fig. 51.** Components in a given operating point of the compensation vector for inverter nonlinearities  $\hat{\mathbf{i}}_{inv}$ , displayed over one fundamental period.

fundamental stator current  $\mathbf{i}_{sl}^{(F)}$  in field coordinates. Its  $i_d$  component characterizes the mutual flux and the  $i_q$  component the load. Both components control the saturation of the machine. The total disturbance vector  $\hat{\mathbf{i}}_{sat}$  is synthesized as the sum of its harmonic components, these being adjusted to their respective phase displacements according to the actual angular position  $\hat{\delta}$  of the revolving fundamental field in the machine.

The respective functions  $f_2(i_{sl})$  and  $f_4(i_{sl})$  for a particular machine are determined in an off-line identification process [28].

The nonlinearity of the PWM inverter, commonly known as dead-time effect, produces distortions of the PWM whenever one of the phase currents changes its sign. With the high-frequency carrier signal superimposed to the modulator input, the stator currents are forced to multiple zero crossings when the fundamental phase currents are close to zero. The effect causes severe current distortions that well-established methods for dead-time compensation cannot handle.

Being time-discrete events, the current distortions are difficult to compensate for in a frequency-domain method. A fairly complex off-line identification method was proposed by Teske and Asher [29] which generates sets of time-variable profiles over one electrical revolution, one profile for every operating point in terms of load and excitation level. The profiles model the nonlinearity effect caused by the high-frequency carrier signals of a particular inverter. Fig. 51 shows the  $d$  and  $q$  components of such a profile as an example, plotted as functions of the fundamental phase angle. During operation of the drive, the appropriate profile

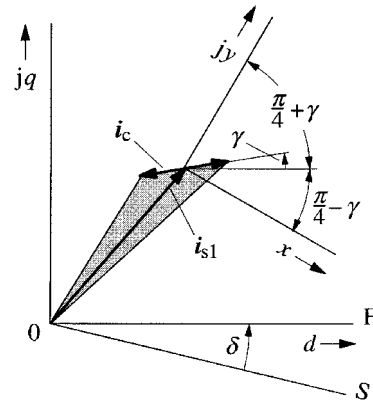


**Fig. 52.** Vector diagram showing the injected ac carrier  $\mathbf{i}_c$  in different reference frames;  $\mathbf{i}_{s1}$ : fundamental current;  $F$ : field-oriented frame;  $S$ : stationary frame.

is retrieved to reconstruct that particular vector  $\hat{\mathbf{i}}_{inv}$  that fits the actual operating point [31].

If the compensation of saturation effects, inverter nonlinearity, and signal unbalance, represented by the respective vectors  $\hat{\mathbf{i}}_{sat}$ ,  $\hat{\mathbf{i}}_{inv}$ , and  $\hat{\mathbf{i}}_u$ , is performed with sufficient accuracy, the remaining signal

$$\hat{\mathbf{i}}_{slot} = \hat{\mathbf{i}}_{slot} e^{j((N/P)\hat{\vartheta} + \hat{\varphi}_{slot})} \quad (80)$$

is not much distorted. This would permit replacing the complex and parameter-dependent PLL structure in Fig. 49 by the simple calculation of the phase angle of  $\hat{\mathbf{i}}_{slot}$  from (80)

$$\hat{\vartheta} = \frac{p}{N} \left( \arctan(\hat{\mathbf{i}}_{slot}) - \hat{\varphi}_{slot} \right). \quad (81)$$

The displacement angle  $\hat{\varphi}_{slot}$  in this equation accounts for the phase shift of the filters used for frequency separation. It is a function of the motor speed [29].

Current publications on revolving carrier methods show that numerous side effects require the signal processing structures to get more and more involved, while the dependence on parameters or on specific off-line commissioning procedures persists.

#### D. Injection of an Alternating Carrier

Revolving carriers scan the whole circumferential profile of anisotropies that exist in a machine. The objective is to determine the characteristics of a particular anisotropy with a view to subsequently identifying its spatial orientation. An alternative class of methods relies on injecting not a rotating but alternating carrier in a specific, though time-variable, spatial direction. The direction is selected in an educated guess to achieve maximum sensitivity in locating the targeted anisotropy. Use is made of already existing knowledge, which is updated by acquiring only an incremental error per sampling period.

1) *Balance of Quadrature Impedances:* The approach of Ha and Sul [32] aims at identifying a field angle while the machine operates at low or zero speed. The principle is explained with reference to Fig. 52. This diagram shows the field-oriented coordinate system  $F$ , which appears displaced by the field angle  $\delta$  as seen from the stationary reference frame  $S$ . A high-frequency ac carrier signal of amplitude  $u_c$





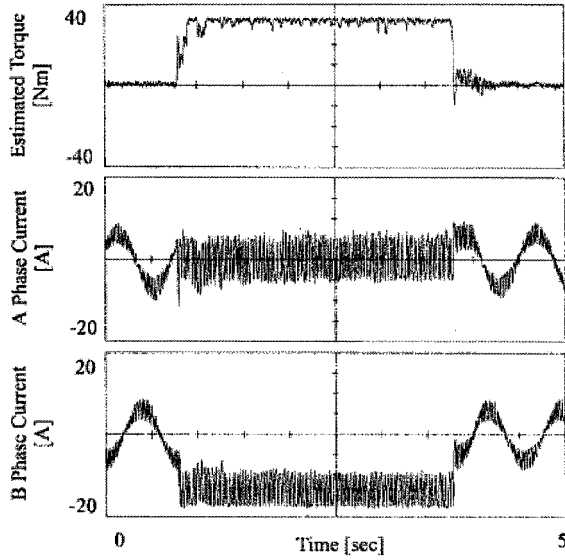


**Fig. 55.** Torque-controlled operation showing the dynamic performance and demonstrating persistent operation at zero stator frequency at 150% of rated torque [33].

carrier voltage of this method is injected at an estimated displacement angle  $\hat{\delta}$  with respect to the true field axis, where  $\hat{\delta}$  deviates from the true field angle  $\delta$  by an error angle  $\gamma_u$  as follows:

$$\hat{\delta} = \delta + \gamma_u. \quad (85)$$

The carrier voltage in stationary coordinates is

$$\mathbf{u}_c^{(S)} = u_c \cos \omega_c t \cdot e^{j\hat{\delta}}. \quad (86)$$

A transformation to field coordinates is done by multiplying (86) by  $\exp(-j\delta)$ , which yields the differential equation

$$\mathbf{u}_c^{(F)} = u_c \cos \omega_c t \cdot e^{j(\hat{\delta}-\delta)} = \mathbf{l}_\sigma^{(F)} \frac{d\mathbf{i}_c}{dt}. \quad (87)$$

The true field angle  $\delta$  in this equation is not known. The excitation at carrier frequency does not interfere with the behavior of the machine at fundamental frequency. Hence, the resulting carrier frequency current  $\mathbf{i}_c$  is only determined by the anisotropic leakage inductance (74), as indicated in the right-hand side of (87).

The solution of (87) is

$$\mathbf{i}_c^{(F)} = \frac{u_c}{\omega_c} \sin \omega_c t \cdot \left( \frac{1}{l_{\sigma d}} \cos(\hat{\delta} - \delta) + j \frac{1}{l_{\sigma q}} \sin(\hat{\delta} - \delta) \right). \quad (88)$$

A multiplication by  $\exp(j\delta)$  transforms this equation back to stationary coordinates.

To gain insight into the physical nature of this current, the harmonic functions are expressed by equivalent complex space vectors. Referring to (85), the result can be written as

$$\mathbf{i}_c^{(S)} = \mathbf{i}_E^+ + \mathbf{i}_E^- \quad (89a)$$

where

$$\begin{aligned} \mathbf{i}_E^+ &= \frac{-j u_c}{4 \omega_c l_{\sigma d} l_{\sigma q}} \left[ (l_{\sigma d} + l_{\sigma q}) e^{j(\omega_c t + \hat{\delta})} \right. \\ &\quad \left. + (l_{\sigma d} - l_{\sigma q}) e^{j(-\omega_c t + \hat{\delta} - 2\gamma_u)} \right] \\ &= \mathbf{i}_p^+ + \mathbf{i}_n^+ \end{aligned} \quad (89b)$$

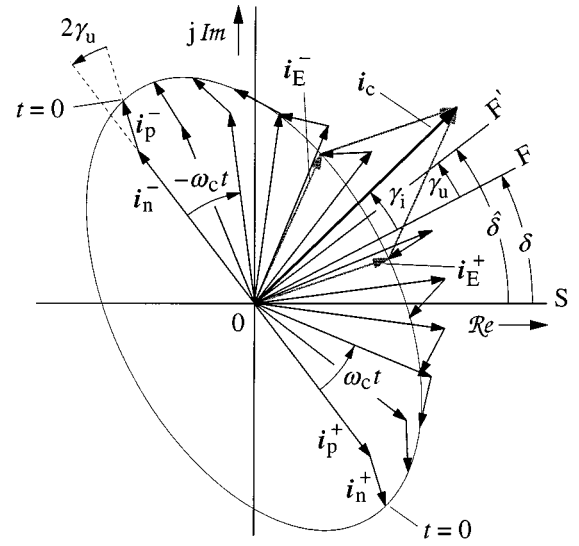


**Fig. 56.** The elliptic trajectories and  $\mathbf{i}_E^+$  and  $\mathbf{i}_E^-$ , created by four circular rotating space vectors;  $S$ : stationary coordinates,  $F$ : field coordinates,  $F'$ : estimated field coordinates.

describes the elliptic trajectory of a current vector that rotates in a positive direction, and

$$\begin{aligned} \mathbf{i}_E^- &= \frac{j u_c}{4 \omega_c l_{\sigma d} l_{\sigma q}} \left[ (l_{\sigma d} + l_{\sigma q}) e^{j(-\omega_c t + \hat{\delta})} \right. \\ &\quad \left. + (l_{\sigma d} - l_{\sigma q}) e^{j(\omega_c t + \hat{\delta} - 2\gamma_u)} \right] \\ &= \mathbf{i}_n^- + \mathbf{i}_p^- \end{aligned} \quad (89c)$$

represents the elliptic trajectory of a negatively rotating current vector. Fig. 56 shows that both elliptic trajectories are congruent. They are composed of current vectors that themselves rotate on circular trajectories in opposite directions. As indicated by (89b), the elliptic trajectory  $\mathbf{i}_E^+$  that develops in a positive direction decomposes into a positive sequence current vector  $\mathbf{i}_p^+$  and a negative sequence current vector  $\mathbf{i}_n^+$ . Similar conditions hold for the trajectory  $\mathbf{i}_E^-$ , building up in a negative direction and being composed, according to (89c), of a positive sequence current vector  $\mathbf{i}_p^-$  and a negative sequence current vector  $\mathbf{i}_n^-$ .

As the true field angle  $\delta$  may not be exactly known, the ac carrier voltage is injected at a spatial displacement  $\gamma_u$  from the true field axis. The direction of the carrier voltage  $\delta + \gamma_u$  coincides with the  $F'$  axis in Fig. 56. Owing to the anisotropy of the machine, the ac carrier current  $\mathbf{i}_c$  deviates spatially from the injected voltage. It develops in the direction  $\delta + \gamma_i$ , where  $|\gamma_i| \geq |\gamma_u|$ . This means that the elliptic trajectories of the current space vectors  $\mathbf{i}_E^+$  and  $\mathbf{i}_E^-$  take their spatial orientation from the existing anisotropy, independent of the direction in which the carrier signal is injected.

The vector diagram in Fig. 56 demonstrates that the geometric additions over time of all space vector components in (89) define the locus of a straight line, inclined at the angle  $\gamma_i$  with respect to the true field axis  $F$ . This circumstance permits identifying the misalignment of the estimated reference frame  $F'$ .

An inspection of the circular space vector components in Fig. 56 shows that the vectors  $\mathbf{i}_p^+$  and  $\mathbf{i}_p^-$ , while rotating in

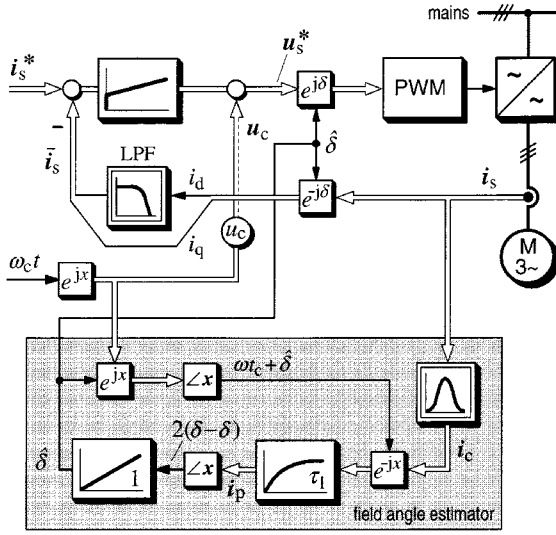


**Fig. 57.** Signal flow graph of a field angle estimation scheme based on the evaluation of elliptic current trajectories.

a positive direction, maintain the constant angular displacement  $2\gamma_u$ . This is indicated for  $t = 0$  in the upper left of Fig. 56. The error angle  $\gamma_u$  can be therefore extracted by rotating the vector  $\mathbf{i}_c$  into a  $-(\omega_c t + \delta)$ -reference frame, in which the sum of the positive rotating vectors appears as a complex dc value

$$\begin{aligned} \mathbf{i}_p &= \mathbf{i}_p^+ + \mathbf{i}_p^- \\ &= \frac{-j u_c}{4\omega_c l_{\sigma d} l_{\sigma q}} \left[ (l_{\sigma d} + l_{\sigma q}) - (l_{\sigma d} - l_{\sigma q}) e^{-j2\gamma_u} \right]. \quad (90) \end{aligned}$$

The remaining components of  $\mathbf{i}_c$  get transformed to a frequency  $2(\omega_c + \omega_s)$  and can be easily suppressed by a low-pass filter.

The signal flow graph Fig. 57 illustrates the field angle estimation scheme. The dc vector  $\mathbf{i}_p$  defined by (90) has as the imaginary part  $-\sin 2\gamma_u$ , which is proportional to the error angle  $\gamma_u = \hat{\delta} - \delta$  for small error values. This signal is sampled at about 1 kHz. It feeds an  $I$ -controller to create the estimated field angle  $\hat{\delta}$  in a closed loop. In doing so, reference is made to the injected carrier signal to build the transformation term  $\omega_c t + \hat{\delta}$ .

As the acquired signal is a dc value in principle, the sampling frequency can be chosen independently from the carrier frequency. This ensures good and dynamically fast alignment with the field axis without the need to choose a high carrier frequency. Also, the dynamics of the speed and torque control system is not impaired as the carrier signal does not appear in the torque building  $q$ -current component. This current component need not be separated by a low-pass filter. Fig. 57 shows that such filter is only provided for the component  $i_d$  in the excitation axis. The SNR of the acquired signal is high, thus permitting operation at a low carrier level. A 100-mA carrier current was found to be sufficient for field angle estimation in a 1-kW drive system. Fig. 58 displays the waveforms of the true and the estimated field angles measured at  $0.004 \omega_{sR}$ , or 6 rpm, and the estimation error that originates from other anisotropies.

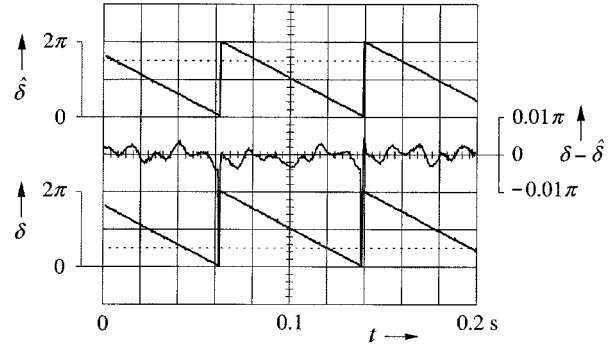


**Fig. 58.** Measured signals from the field angle estimation scheme in Fig. 57, operated at  $0.004 \omega_{sR}$ ; from the top: estimated field angle, estimation error, and true field angle.

### E. High-Frequency Excitation by PWM Switching

The switching of a PWM inverter subjects the machine to repetitive transient excitation. The resulting changes of the machine currents depend, in addition to the applied voltages and the back EMF, also on machine anisotropies. Appropriate signal acquisition and processing permits extracting a characteristic component of the anisotropy in that particular phase axis in which a switching has occurred. To reconstruct the complete spatial orientation of an anisotropy therefore requires the evaluation of a minimum of two switching events in different phase axes. The switchings must be executed within a very short time interval such that the angular orientation of the anisotropy remains almost unchanged.

Other than continuous carrier injection methods, which are frequency-domain methods, PWM excitation constitutes a sequence of nonperiodic time-discrete events and hence requires time-domain methods for signal processing. The absence of spectral filters enables a faster dynamic response. Another basic difference is that the high-frequency process cannot be seen as being independent from the fundamental frequency behavior of the machine. This requires using the complete machine model for the analysis.

1) *The INFORM Method:* Schroedl [35] calls his approach the *INFORM* method (indirect flux detection by on-line reactance measurement). The analysis starts from the stator voltage equation (10a) in stator coordinates,  $\omega_s = 0$ , as

$$\mathbf{u}_s^{(S)} = r_\sigma \mathbf{i}_s + \mathbf{l}_\sigma^{(S)} \frac{d\mathbf{i}_s}{d\tau} + \frac{k_r}{\tau_r} (j\omega\tau_r - 1)\boldsymbol{\psi}_r \quad (91)$$

where the tensor  $\mathbf{l}_\sigma^{(S)}$  models the saturation-induced anisotropy. The rate of change  $d\mathbf{i}_s/d\tau$  of the stator current vector is measured as a difference  $\Delta\mathbf{i}_s$  over a short time interval  $\Delta\tau$  and with a constant switching state vector applied as  $\mathbf{u}_s$ . The influence on  $\Delta\mathbf{i}_s$  of the resistive voltage  $r_\sigma \mathbf{i}_s$  and the back EMF is eliminated by taking two consecutive measurements while applying two switching state vectors in opposite directions, e.g.,  $\mathbf{u}_1$  and  $\mathbf{u}_4 = -\mathbf{u}_1$  in Fig. 59, each for a time interval  $\Delta\tau$ . It can be assumed that the fundamental components of  $\mathbf{i}_s$  and  $\boldsymbol{\psi}_s$  do not change between two measurements.

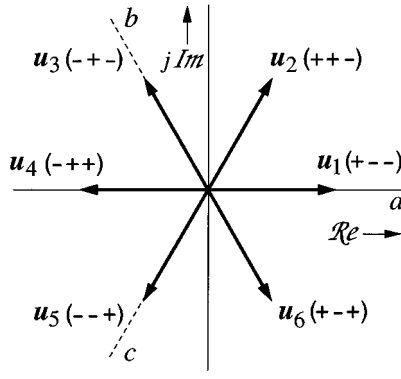


**Fig. 59.** The active switching state vectors  $\mathbf{u}_1$  to  $\mathbf{u}_6$ , representing the stator voltages at pulsewidth modulation;  $a$ ,  $b$  and  $c$  denote the phase axes. The signs of the phase potentials are indicated in brackets.

Inserting the two switching state vectors  $\mathbf{u}_1$  and  $\mathbf{u}_4$  separately in (91) and taking the difference of the two resulting equations yields

$$\mathbf{u}_1 - \mathbf{u}_4 = \mathbf{l}_\sigma \left( \frac{\Delta \dot{\mathbf{i}}_s^{(\mathbf{u}_1)}}{\Delta \tau} - \frac{\Delta \dot{\mathbf{i}}_s^{(\mathbf{u}_4)}}{\Delta \tau} \right). \quad (92)$$

Of interest in this equation are the components of the current changes in the spatial direction of the transient excitation, which is the  $a$  axis when  $\mathbf{u}_1$  and  $\mathbf{u}_4$  are used (see Fig. 59). Therefore, after multiplying (92) by the inverse, as shown in (93) at the bottom of the page, of the leakage inductance tensor and taking the  $a$ -component of the result, we obtain

$$\begin{aligned} \Delta i_a^{(\mathbf{u}_1)} - \Delta i_a^{(\mathbf{u}_4)} &= \mathbf{l}_\sigma^{-1} 2u_s \Delta \tau \\ &= [(l_{\sigma d} + l_{\sigma q}) - (l_{\sigma d} - l_{\sigma q}) \cos 2\delta] u_s \Delta \tau \end{aligned} \quad (94a)$$

where the  $\Delta i_a$  are the respective changes of the  $a$ -phase current, and  $u_s$  is the magnitude of the switching state vectors.

The  $b$ -axis anisotropy component is obtained by acquiring the changes  $\Delta i_b$  following transient excitations by  $\mathbf{u}_3$  and  $\mathbf{u}_6 = -\mathbf{u}_3$  (Fig. 59). The derivation is done in a similar manner as with (94a), but the resulting equation is rotated into the excitation axis, multiplying it by  $\exp(-2\pi/3)$  to yield

$$\begin{aligned} \Delta i_c^{(\mathbf{u}_3)} - \Delta i_c^{(\mathbf{u}_6)} &= [(l_{\sigma d} + l_{\sigma q}) - (l_{\sigma d} - l_{\sigma q}) \\ &\quad \cdot \cos 2 \left( \delta - \frac{2\pi}{3} \right)] u_s \Delta \tau. \end{aligned} \quad (94b)$$

The  $c$ -axis anisotropy is detected using  $\mathbf{u}_5$  and  $\mathbf{u}_2 = -\mathbf{u}_5$  as excitations, and  $\exp(-4\pi/3)$  as the rotation term

$$\begin{aligned} \Delta i_b^{(\mathbf{u}_5)} - \Delta i_b^{(\mathbf{u}_2)} &= [(l_{\sigma d} + l_{\sigma q}) - (l_{\sigma d} - l_{\sigma q}) \\ &\quad \cdot \cos 2 \left( \delta - \frac{4\pi}{3} \right)] u_s \Delta \tau. \end{aligned} \quad (94c)$$

The phase current changes expressed by (94) are now added, aligning them with the real axis by the respective weights 1,  $a^2$ , and  $a$  as

$$\mathbf{f} = \frac{2}{3} \left[ \Delta i_a^{(\mathbf{u}_1)} - \Delta i_a^{(\mathbf{u}_4)} + a^2 \left( \Delta i_b^{(\mathbf{u}_3)} - \Delta i_b^{(\mathbf{u}_6)} \right) + a \left( \Delta i_c^{(\mathbf{u}_5)} - \Delta i_c^{(\mathbf{u}_2)} \right) \right]. \quad (95)$$

The result is a field position vector

$$\mathbf{f} = \frac{1}{2} (l_{\sigma d} - l_{\sigma q}) u_s \Delta \tau e^{j(2\hat{\delta} + \pi)} \quad (96)$$

which can be proven by solving (92) for the respective current changes and inserting these into (96).

The vector  $\mathbf{f}(\Delta \dot{\mathbf{i}}_s)$  can be computed online from the measured current changes. Its argument is the double field angle, phase-shifted by a constant displacement  $\pi$ . Hence

$$\hat{\delta} = \frac{\arg(\mathbf{f}) - \pi}{2} \quad (97)$$

represents the estimated field angle. The controlled machine should have closed rotor slots. The slot covers shield the rotor bars from the high-frequency leakage fields and thus reduce, but not completely eliminate, the disturbance caused by the slotting anisotropy.

2) *Instantaneous Rotor Position Measurement:* While the rotor slot anisotropy acts as a disturbance to the field angle identification methods, this anisotropy can be exploited to identify the rotor position angle. Magnetic saturation then takes the role of the disturbance. The method developed by Jiang [36] relies on the instantaneous measurement of the total leakage inductances per stator phase.

Fig. 60 introduces the physical background, displaying schematically an induction motor having only two rotor bars. It is assumed in Fig. 60(a) that only stator phase  $a$  is energized, creating a flux density distribution  $B_a(\alpha)$  as shown in Fig. 60(b). The graph below shows the location of the rotor bars at a phase displacement angle  $\vartheta$ , which is the unknown rotor position angle. It is obvious that the flux linkage  $\psi_r$  of this rotor winding reduces as  $\vartheta$  increases, rising again for  $\vartheta > \pi$  [Fig. 60(d)]. The mutual inductance  $m_{s1} = \psi_r / i_s$  between the stator and the rotor windings changes in direct proportion. The total leakage inductance of stator phase  $a$  is then computed as

$$l_{\sigma a} = l_s \left( 1 - \frac{m_{s1}^2}{l_s l_1} \right) \quad (98)$$

where  $l_s$  and  $l_1$  are the inductances of the stator winding and of the single rotor winding, respectively. Fig. 60(e) shows how the total leakage inductance  $l_{\sigma a}$  varies as a function of the rotor position angle  $\vartheta$ .

According to (98), the total leakage inductance depends on the square of the mutual inductance, which is also true if more than two rotor bars exist [27]. Therefore, a rotor having  $N$  rotor bars shows a similar characteristic as in Fig. 60(e), but with  $N$  maximum values. The total leakage inductances

$$\mathbf{l}_\sigma^{-1(s)} = \frac{1}{l_{\sigma d} l_{\sigma q}} \begin{bmatrix} \frac{1}{2} (l_{\sigma d} + l_{\sigma q}) - \frac{1}{2} (l_{\sigma d} - l_{\sigma q}) \cos 2\delta & \frac{1}{2} (l_{\sigma d} - l_{\sigma q}) \sin 2\delta \\ \frac{1}{2} (l_{\sigma d} - l_{\sigma q}) \sin 2\delta & \frac{1}{2} (l_{\sigma d} + l_{\sigma q}) + \frac{1}{2} (l_{\sigma d} - l_{\sigma q}) \cos 2\delta \end{bmatrix} \quad (93)$$

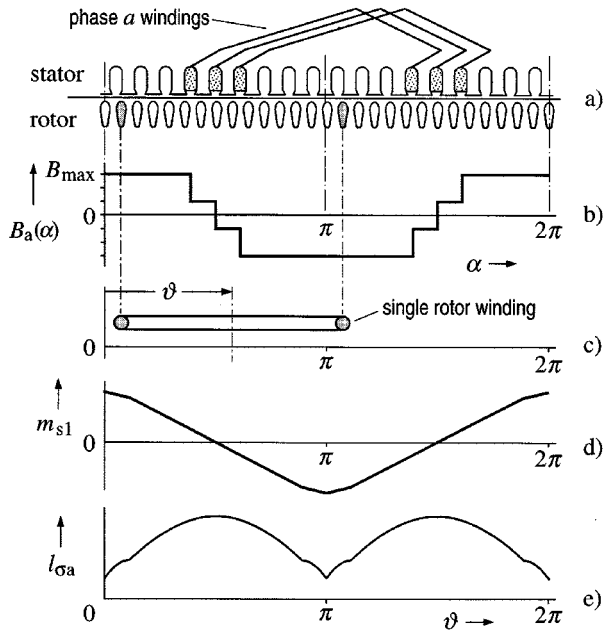


**Fig. 60.** Distributions in a two-slot machine with only phase  $a$  energized. (a) Energized stator windings. (b) Flux density distribution. (c) Location of the two rotor bars. (d) Mutual inductance between stator and rotor winding. (e) Total leakage inductance of stator winding phase  $a$ .

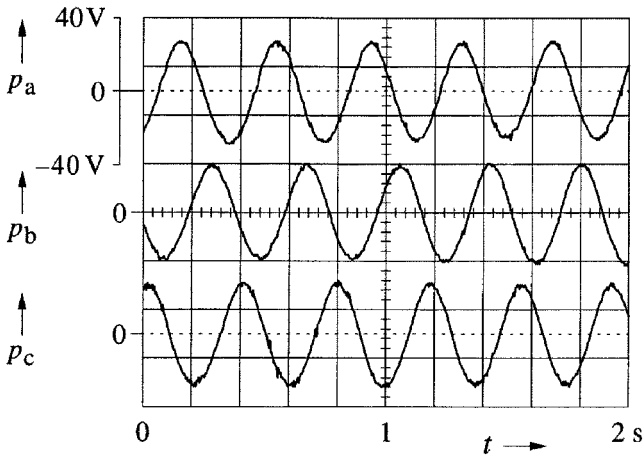


**Fig. 61.** Phase components  $p_a$ ,  $p_b$ , and  $p_c$  of the position vector measured at 0.1 Hz stator frequency.

of the other phases,  $l_{\sigma b}$  and  $l_{\sigma c}$ , change in a similar manner. They depend on the respective positions of the rotor winding, as seen from the winding axes  $b$  and  $c$ . Since  $N$  is generally not a multiple of three, the curves  $l_{\sigma a}(\vartheta)$ ,  $l_{\sigma b}(\vartheta)$ , and  $l_{\sigma c}(\vartheta)$  are phase shifted with respect to each other by  $2\pi/3$ . Fig. 61 shows the respective signals, measured at 0.1 Hz stator frequency and interpreted as the position signals  $p_a$ ,  $p_b$ , and  $p_c$  versus time. In a favorable manner, the finite widths of the rotor bars and the rotor slots tend to blur the sharp edges that are seen in Fig. 60(e), which is a curve simulated with infinite thin conductor diameters.

The method to measure the position signals is explained with reference to a condition where the switching state  $\mathbf{u}_1$  has been turned on. The three motor terminals are then forced by the dc link voltage  $u_d$  to the respective potentials  $u_a = u_d/2$

and  $u_b = u_c = -u_d/2$ , or  $(+ - -)$  as symbolically indicated in Fig. 59. The following approximative stator voltage equations can be established:

$$u_d = l_{\sigma a} \frac{di_a}{d\tau} + u_{ia} - l_{\sigma b} \frac{di_b}{d\tau} - u_{ib} \quad (99)$$

$$u_d = l_{\sigma a} \frac{di_a}{d\tau} + u_{ia} - l_{\sigma c} \frac{di_c}{d\tau} - u_{ic} \quad (100)$$

which are solved considering the constraint  $i_a + i_b + i_c = 0$  and assuming that the rotor induced voltages form a zero sequence system

$$u_{ia} + u_{ib} + u_{ic} = 0. \quad (101)$$

These conditions permit summing the three phase voltages to form an unbalanced voltage

$$u_{\sigma} = u_a + u_b + u_c \quad (102)$$

where  $u_a = l_{\sigma a} di_a/d\tau + u_{ia}$ , while the phase voltages  $u_b$  and  $u_c$  are expressed likewise. The result is

$$u_{\sigma}^{(1)} = \frac{\begin{bmatrix} u_d(l_{\sigma a}l_{\sigma b} + l_{\sigma a}l_{\sigma c} - 2l_{\sigma b}l_{\sigma c}) \\ +(-u_{ia})(l_{\sigma a}l_{\sigma b} + l_{\sigma a}l_{\sigma c} - 2l_{\sigma b}l_{\sigma c}) \\ +(-u_{ib})(l_{\sigma b}l_{\sigma c} + l_{\sigma b}l_{\sigma a} - 2l_{\sigma a}l_{\sigma c}) \\ +(-u_{ic})(l_{\sigma c}l_{\sigma a} + l_{\sigma c}l_{\sigma b} - 2l_{\sigma a}l_{\sigma b}) \end{bmatrix}}{l_{\sigma a}l_{\sigma b} + l_{\sigma b}l_{\sigma c} + l_{\sigma a}l_{\sigma c}} \quad (103)$$

where the superscript (1) refers to the actual switching state vector  $\mathbf{u}_1$ .

The induced voltages  $u_i$  are small at lower speeds, which permits neglecting the last three terms in the numerator of (103), especially since (101) further reduces their influence. What remains is interpreted as the  $a$ -component of a rotor position vector  $\mathbf{p}(\vartheta_N)$

$$p_a(\vartheta_N) = u_d \frac{l_{\sigma a}l_{\sigma b} + l_{\sigma a}l_{\sigma c} - 2l_{\sigma b}l_{\sigma c}}{l_{\sigma a}l_{\sigma b} + (l_{\sigma a} + l_{\sigma b})l_{\sigma c}} \quad (104)$$

as it depends only on the phase values of the leakage inductances, if  $u_d$  is constant. Note that  $p_a(\vartheta_N) = u_{\sigma}^{(1)}$  is obtained by instantaneous sampling of the phase voltages (102) as a speed-independent value.

The angle  $\vartheta_N$  indicates the angular position of the rotor within one rotor slot pitch. Hence a full mechanical revolution occurs when  $\vartheta_N/N$  increments by  $2\pi$ , and the time interval displayed in Fig. 61 corresponds to an angular rotor displacement of five rotor slots.

The same expression (104) can be also derived without approximation, taking the difference  $u_{\sigma}^{(1)} - u_{\sigma}^{(4)} = 2p_a(\vartheta_N)$  of two sampled voltages from opposite switching state vectors [27]. This eliminates the disturbing influence of the induced voltages  $u_i$  at higher speed.

Taking additional measurements of  $u_{\sigma}$  while, for instance, the switching state vector  $\mathbf{u}_3$  is turned on permits calculating the  $b$  component  $p_b$ . The  $c$  component  $p_c$  results from a sample with  $\mathbf{u}_5$  being active. Alternatively, a sample at  $\mathbf{u}_2$  yields the value  $-p_c$  since  $\mathbf{u}_2$  aligns with the negative  $c$  axis (Fig. 59). Three different voltage samples are used to compute the complex rotor position vector

$$\mathbf{p}(\vartheta_N) = \frac{2}{3} (p_a(\vartheta_N) + a p_b(\vartheta_N) + a^2 p_c(\vartheta_N)) = p_{\alpha} + j p_{\beta} \quad (105)$$

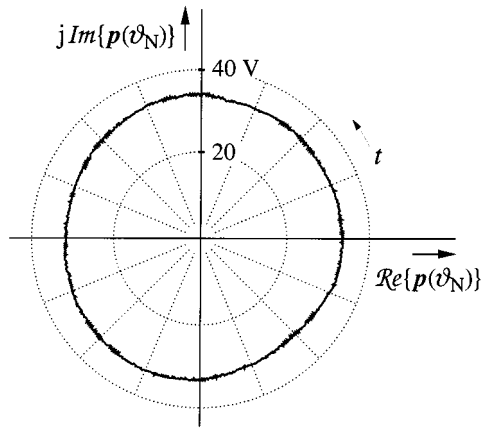


**Fig. 62.** Measured trajectory  $\mathbf{p}(\delta_N)$  of the complex rotor position vector recorded over  $1/N$ th of a full mechanical revolution of the motor shaft.  $N$ : number of rotor bars.

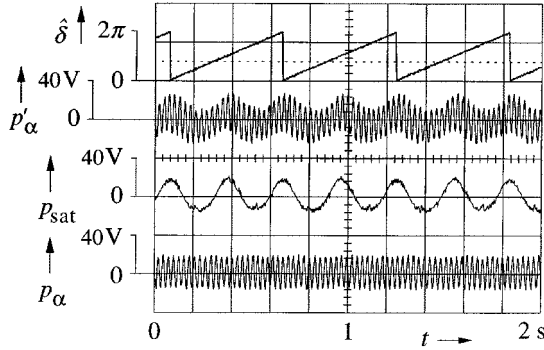


**Fig. 63.** From top: estimated field angle  $\hat{\delta}$ , acquired signal  $p'_\alpha$ , saturation component  $p_{\text{sat}}$ , and extracted position signal  $p_\alpha$ .

an oscillogram of which is shown in Fig. 62. A full revolution of  $\mathbf{p}(\vartheta_N)$  indicates an angular rotor displacement of one rotor slot pitch. This emphasizes the high spatial resolution that this method provides. Also noteworthy is the high level of the acquired signals, which is around 35 V.

To establish a sensorless speed control system, the field angle is derived from the rotor position  $\vartheta = \vartheta_N/N$  by adding the slip angle obtained from the condition (29) for rotor field orientation

$$\hat{\delta} = p \frac{\vartheta_N}{N} + \frac{l_m}{\tau_r} \int \frac{i_q}{\psi_{rd}} d\tau \quad (106)$$

where  $p$  is the number of pole pairs. The state variables under the integral in (106) are estimated by the rotor model (28).

The field angle (106) can further serve to eliminate the saturation-induced disturbance of the position signals. It introduces low-frequency components that superimpose on the measured signal  $p'_\alpha$  in Fig. 63 if the machine is saturated. The saturation components are in synchronism with the varying field angle  $\delta$ . An adaptive spatial low-pass filter, controlled by the estimated field angle  $\hat{\delta}$ , extracts the saturation component  $p_{\text{sat}}$  from the distorted signal  $p'_\alpha$ , permitting the calculation of an undisturbed position signal  $p_\alpha = p'_\alpha - p_{\text{sat}}$ , which is shown in the lowest trace of Fig. 63.

Rotor position acquisition is possible at sampling rates of several kilohertz [27]. The spatial resolution and the SNR are

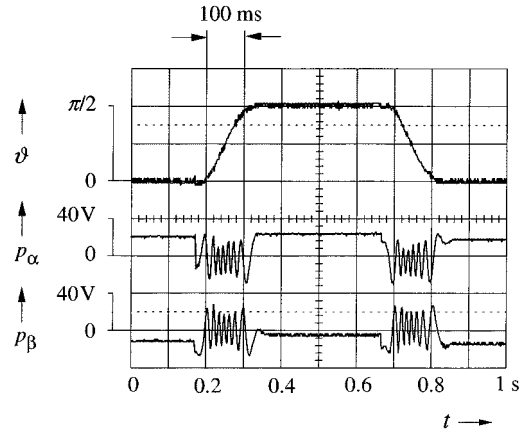


**Fig. 64.** Sensorless position control showing a repetitive motor shaft displacement of  $\pm 90^\circ$  at 120% rated transient torque; traces from top: motor shaft angle  $\vartheta$ , rotor position signals  $p_\alpha$ , and  $p_\beta$ .

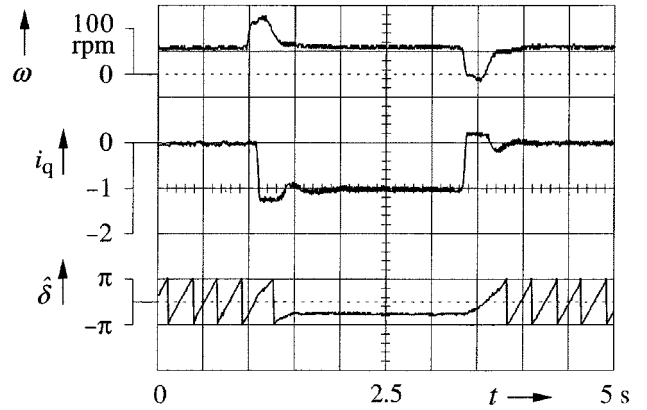


**Fig. 65.** Persistent operation at zero stator frequency with 120% rated torque applied. Positioning transients initiate and terminate the steady-state intervals. Traces from top: mechanical speed  $\omega$ , normalized torque-building current  $i_q$ , and estimated field angle  $\hat{\delta}$ .

very high. This permits implementing precise incremental positioning systems for high dynamic performance. However, the incremental position is lost at higher speeds when the frequency of the position signal becomes higher than twice the sampling frequency.

The oscillogram in Fig. 64 shows a positioning cycle that requires maximum dynamics at 120% rated torque. The high magnetic saturation during the acceleration intervals temporarily reduces the amplitude of the position signals; the position accuracy remains unaffected, as the relevant information is contained in the phase angles.

Fig. 65 demonstrates persistent speed-controlled operation at zero stator frequency, interspersed with high dynamic changes. The drive operates initially at no-load at about 60 rpm, which is the slip speed that corresponds to 120% rated torque. Such torque level is then applied in a negative direction, which forces the machine to operate at zero stator frequency in order to maintain the speed at its commanded level. Short dynamic overshoots occur when the load is applied and subsequently released. The lowest trace shows that the rotor field remains in a fixed position while the load is applied.



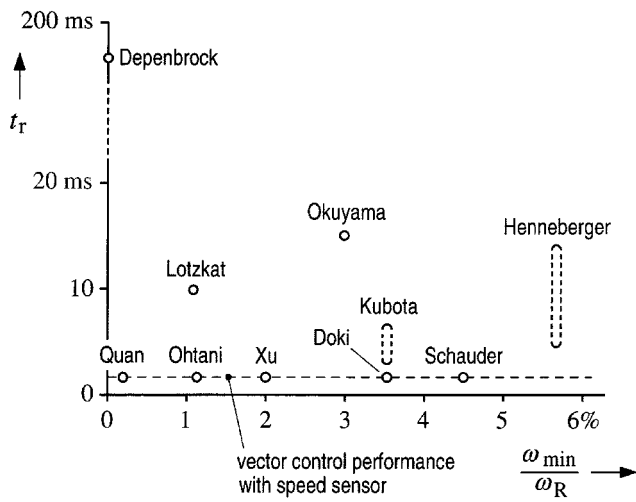


**Fig. 66.** Performance comparison of speed-sensorless drive control methods, excluding carrier injection methods. The diagram displays torque rise time  $t_r$  versus minimum speed  $\omega_{\min}$ .

## IX. SUMMARY AND PERFORMANCE COMPARISON

A large variety of sensorless controlled ac drive schemes are used in industrial applications. Open-loop control systems maintain the stator voltage-to-frequency ratio at a predetermined level to establish the desired machine flux. They are particularly robust at very low and very high speeds but satisfy only low or moderate dynamic requirements. Small load-dependent speed deviations can be compensated for by incorporating a speed or rotor frequency estimator.

High-performance vector control schemes require a flux vector estimator to identify the spatial location of the magnetic field. Field-oriented control stabilizes the tendency of induction motors to oscillate at transients, which enables fast control of torque and speed. The robustness of a sensorless ac drive can be improved by adequate control structures and by parameter identification techniques. Depending on the used method, sensorless control can be achieved over a base speed range of 1 : 100 to 1 : 150 at very good dynamic performance. Stable and persistent operation at zero stator frequency can be established even when using the fundamental model of the machine, provided that all drive system components are accurately modeled and their parameters correctly adapted to the corresponding system values. Accurate speed estimation in this region, however, is difficult since the fundamental model becomes unobservable. A fast speed transition through zero stator frequency can be achieved without employing sophisticated algorithms.

The steady-state speed accuracy depends on the accurate adjustment of the rotor time constant in the estimation model. Very high-speed accuracy can be achieved by exploiting the rotor slot effect for parameter adaptation. Since cost is an important issue, algorithms that can be implemented in standard microcontroller hardware are preferred for industrial applications.

The graph in Fig. 66 gives a comparison of different methods for speed sensorless control in terms of the torque rise time  $t_r$  and the low-speed limit of stable operation. The data are taken from the cited references; the results should

be considered approximate, since the respective test and evaluation conditions may differ. Only methods that use the fundamental machine model are compared in Fig. 65.

Improved low-speed performance can be achieved by exploiting the anisotropic properties of induction motors. The spatial orientations of such anisotropies are related to the field angle and to the mechanical rotor position. They can be identified either by injecting high-frequency carrier signals into the stator windings and process the response of the machine or by making use of the transients that a PWM inverter generates. These methods have recently emerged, and they bear great promise for the development of universally applicable sensorless ac motor drives.

## APPENDIX NORMALIZATION

The base variables are the nominal per-phase values of voltage and current as follows:

at star connection

$$U_{phR} = \frac{1}{\sqrt{3}} U_R \quad \text{and} \quad I_{phR} = I_R$$

at delta connection

$$U_{phR} = U_R \quad \text{and} \quad I_{phR} = \frac{1}{\sqrt{3}} I_R.$$

The normalization values are the respective peak amplitudes. They are given for

voltage	$\sqrt{2} U_{phR}$	flux linkage	$\frac{\sqrt{2} \cdot U_{phR}}{\omega_{sR}}$
current	$\sqrt{2} I_{phR}$	power	$3 U_{phR} I_{phR}$
impedance	$\frac{U_{phR}}{I_{phR}}$	torque	$3p \frac{U_{phR} I_{phR}}{\omega_{sR}}$
inductance	$\frac{U_{phR}}{\omega_{sR} \cdot I_{phR}}$	speed	$\frac{\omega_{sR}}{p}$
time	$\frac{1}{\omega_{sR}}$		

*Example:* Faradays Law  $'u = d'\psi/dt$ , where the string quote “'” before the variable denotes a nonnormalized value.

The equation is normalized as

$$\frac{'u}{\sqrt{2} U_{phR}} = \frac{d}{d(\omega_{sR} t)} \cdot \frac{'\psi}{\frac{1}{\omega_{sR}} \cdot \sqrt{2} \cdot U_{phR}}$$

to yield

$$u = \frac{d\psi}{d\tau}.$$

## REFERENCES

- [1] K. Rajashekara, A. Kawamura, and K. Matsuse, Eds., *Sensorless Control of AC Motors*. Piscataway, NJ: IEEE Press, 1996.
- [2] P. K. Kovács and E. Rácz, *Transient Phenomena in Electrical Machines* (in German). Budapest, Hungary: Verlag der Ungarischen Akademie der Wissenschaften, 1959.
- [3] J. Holtz, “The representation of AC machine dynamics by complex signal flow graphs,” *IEEE Trans. Ind. Electron.*, vol. 42, pp. 263–271, June 1995.

- [4] —, "Pulsewidth modulation for electronic power converters," *Proc. IEEE*, vol. 82, pp. 1194–1214, Aug. 1994.
- [5] —, "On the spatial propagation of transient magnetic fields in AC machines," *IEEE Trans. Ind. Applicat.*, vol. 11, pp. 483–488, Sept./Oct. 1975.
- [6] A. Abbondanti and M. B. Brennen, "Variable speed induction motor drives use electronic slip calculator based on motor voltages and currents," *IEEE Trans. Ind. Applicat.*, vol. 29, pp. 344–348, Mar./Apr. 1993.
- [7] W. Lotzkat, "Industrial low-cost PWM inverter drives with ride-through capability," Ph.D. dissertation (in German), Wuppertal Univ., Wuppertal, Germany, 1991.
- [8] F. Blaschke, "The principle of field orientation as applied to the new transvector closed loop control system in a PWM inverter induction motor drive," *Siemens Rev.*, vol. 39, no. 5, pp. 217–220, 1972.
- [9] C. Schauder, "Adaptive speed identification for vector control of induction motors without rotational transducers," in *IEEE Industry Applications Soc. Annu. Meeting*, San Diego, CA, 1989, pp. 493–499.
- [10] F. Z. Peng, T. Fukao, and J. S. Lai, "Robust speed identification for speed-sensorless vector control of induction motors," *IEEE Trans. Ind. Applicat.*, vol. 30, pp. 1234–1240, Sept./Oct. 1994.
- [11] T. Okuyama, N. Fujimoto, T. Matsui, and Y. Kubota, "A high performance speed control scheme for induction motor without speed and voltage sensors," in *IEEE Industry Applications Soc. Annu. Meeting*, Denver, CO, 1986, pp. 106–111.
- [12] T. Ohtani, N. Takada, and K. Tanaka, "Vector control of induction motor without shaft encoder," *IEEE Trans. Ind. Applicat.*, vol. 28, pp. 157–165, Jan./Feb. 1992.
- [13] H. Kubota, K. Matsuse, and T. Nakano, "DSP based speed adaptive flux observer of induction motor," *IEEE Trans. Ind. Applicat.*, vol. 29, pp. 344–348, Mar./Apr. 1993.
- [14] S. Doki, S. Sangwongwanich, T. Yonemoto, and S. Okuma, "Speed-sensorless field-oriented vector control using adaptive sliding observers," in *IECON, 16th Annu. Conf. IEEE Industrial Electronics Soc.*, Asilomar, CA, 1990, pp. 453–458.
- [15] Y.-R. Kim, S.-K. Sul, and M.-H. Park, "Speed sensorless vector control of induction motor using extended Kalman filter," *IEEE Trans. Ind. Applicat.*, vol. 30, pp. 1225–1233, Sept./Oct. 1994.
- [16] G. Henneberger, B. J. Brunsbach, and Th. Klepsch, "Field oriented control of synchronous and asynchronous drives without mechanical sensors using a Kalman-filter," in *Eur. Conf. Power Electronics and Applications EPE*, Florence, Italy, 1991, pp. 3/664–3/671.
- [17] H. Tajima and Y. Hori, "Speed sensor-less field-orientation control of the induction machine," *IEEE Trans. Ind. Applicat.*, vol. 29, pp. 175–180, Jan./Feb. 1993.
- [18] X. Xu and D. W. Novotny, "Implementation of direct stator flux oriented control on a versatile DSP based system," *IEEE Trans. Ind. Applicat.*, vol. 29, pp. 694–700, Mar./Apr. 1991.
- [19] J. Holtz and A. Khambadkone, "Vector controlled induction motor drive with a self-commissioning scheme," *IEEE Trans. Ind. Electron.*, vol. 38, pp. 322–327, 1991.
- [20] J. Jiang and J. Holtz, "High dynamic speed sensorless AC drive with on-line parameter tuning and steady-state accuracy," *IEEE Trans. Ind. Electron.*, vol. 44, pp. 240–246, Mar./Apr. 1997.
- [21] J. Holtz and J. Quan, "Sensorless vector control of induction motors at very low speed using a nonlinear inverter model and parameter identification," in *IEEE Industry Applications Soc. Annu. Meeting*, Chicago, IL, Sept. 30–Oct. 4, 2001.
- [22] Th. Frenze, F. Hoffman, and H. G. Langer, "Speed sensorless control of traction drives—Experiences on vehicles," in *8th Eur. Conf. Power Electronics and Applications EPE*, Lausanne, Switzerland, 1999, CD ROM.
- [23] H. Kubota and K. Matsuse, "Speed sensorless field oriented control of induction motor with rotor resistance adaptation," *IEEE Trans. Ind. Applicat.*, vol. 30, pp. 1219–1224, Sept./Oct. 1994.
- [24] M. Depenbrock, "Eur. Conf. Power Electronics and Applications," Lausanne, Switzerland, CD-ROM, 1999.
- [25] M. W. Degner and R. D. Lorenz, "Using multiple saliencies for the estimation of flux, position and velocity in AC machines," *IEEE Trans. Ind. Applicat.*, vol. 34, pp. 1097–1104, Sept./Oct. 1998.
- [26] J. Cilia, D. M. Asher, and K. J. Bradley, "Sensorless position detection for vector controlled induction motor drives using an asymmetric outer-section cage," *IEEE Trans. Ind. Applicat.*, vol. 33, pp. 1162–1169, Sept./Oct. 1997.
- [27] J. Holtz, "Sensorless position control of induction motors—An emerging technology," *IEEE Trans. Ind. Electron.*, vol. 45, pp. 840–852, Dec. 1998.
- [28] N. Teske, G. M. Asher, M. Sumner, and K. J. Bradley, "Suppression of saturation saliency effects for the sensorless position control of induction motor drives under loaded conditions," *IEEE Trans. Ind. Electron.*, vol. 47, pp. 1142–1149, Oct. 2000.
- [29] N. Teske, G. M. Asher, K. J. Bradley, and M. Sumner, "Analysis and suppression of inverter clamping saliency in sensorless position controlled of induction motor drives," in *IEEE Industry Applications Soc. Annu. Meeting*, Chicago, IL, Sept. 30–Oct. 4, 2001, CD ROM.
- [30] F. Briz, A. Diez, and M. W. Degner, "Dynamic operation of carrier-signal-injection-based sensorless direct field-oriented AC drives," *IEEE Trans. Ind. Applicat.*, vol. 36, pp. 1360–1368, Sept./Oct. 2000.
- [31] N. Teske, G. M. Asher, K. J. Bradley, and M. Sumner, "Encoderless position control of induction machines," in *9th Eur. Conf. Power Electronics and Applications EPE*, CD-ROM, Graz, Austria, 2001.
- [32] J.-I. Ha and S.-K. Sul, "Sensorless field-oriented control of an induction machine by high-frequency signal injection," *IEEE Trans. Ind. Applicat.*, vol. 35, pp. 45–51, Jan./Feb. 1999.
- [33] B.-H. Bae, G.-B. Kim, and S.-K. Sul, "Improvement of low speed characteristics of railway vehicle by sensorless control using high frequency injection," in *IEEE Industry Applications Soc. Annu. Meeting*, CD-ROM, Rome, Italy, Oct. 2000.
- [34] M. Linke, R. Kennel, and J. Holtz, "Sensorless speed and position control of permanent magnet synchronous machines," in *IECON, 28th Annu. Conf. IEEE Industrial Electronics Soc.*, Sevilla, Spain, 2002.
- [35] M. Schroedl, "Sensorless control of AC machines at low speed and standstill based on the inform method," in *IEEE Industry Applications Soc. Annu. Meeting*, Pittsburgh, PA, Sept. 30–Oct. 4, 1996, pp. 270–277.
- [36] J. Jiang, "Sensorless field oriented control of induction motors at zero stator frequency," Ph.D. dissertation (in German), Wuppertal Univ., Wuppertal, Germany, 1999.
- [37] P. K. Kovács and E. Rácz, *Transient Phenomena in Electrical Machines*. Amsterdam, The Netherlands: Elsevier, 1984.



**Joachim Holtz** (Fellow, IEEE) graduated in 1967 and received the Ph.D. degree from the Technical University of Braunschweig, Braunschweig, Germany, in 1969.

In 1969, he became an Associate Professor and, in 1971, he became a Full Professor and Head of the Control Engineering Laboratory, Indian Institute of Technology, Madras, India. In 1972, he joined the Siemens Research Laboratories, Erlangen, Germany. From 1976 to 1998, he was a Professor and Head of the Electrical Machines and Drives Laboratory, Wuppertal University, Wuppertal, Germany. He is currently a Government Advisor and a consultant to various international industries. He has authored more than 100 technical papers, including 70 refereed publications in journals. He has also authored 17 invited conference papers and 10 invited papers published in journals. He is the coauthor of four books and holds 29 patents.

Dr. Holtz was the recipient of the IEEE Industrial Electronics Society Dr. Eugene Mittelmann Achievement Award, the IEEE Industrial Applications Society Outstanding Achievement Award, the IEEE Power Electronics Society William E. Newell Field Award, the IEEE Third Millennium Medal, and the IEEE Lamme Gold Medal. He has earned six IEEE Prize Paper Awards. He is Past Editor-in-Chief of the IEEE TRANSACTIONS ON INDUSTRIAL ELECTRONICS, a Distinguished Lecturer of the IEEE Industrial Applications Society and IEEE Industrial Electronics Society, a Senior AdCom Member of the IEEE Industrial Electronics Society, and a member of Static Power Converter Committee of the IEEE Industrial Applications Society.